Draft date 27th July, 2017
submitted to MNRAS on 17 May 2017

THE SAMI GALAXY SURVEY: DATA RELEASE ONE WITH EMISSION-LINE PHYSICS VALUE-ADDED PRODUCTS

Andrew W. Green†,[1] Scott M. Croom,[2,3] Nicholas Scott,[2] Luca Cortese,[4] Anne M. Medling,[5,6,7] Francesco D'Eugenio,[3,5] Julia J. Bryant,[1,2,3] Joss Bland-Hawthorn,[2] J. T. Allen,[2,3] Rob Sharp,[5] I-Ting Ho,[8] Brent Groves,[5] Michael J. Drinkwater,[9,3] Elizabeth Mannering,[1] Lloyd Harischandra,[1] Jesse van de Sande,[2] Adam D. Thomas,[5] Simon O'Toole,[1] Richard M. McDermid,[1,10] Minh Vuong,[1] Katrina Sealey,[1] Amanda E. Bauer,[1] S. Brough,[11] Barbara Catinella,[4] Gerald Cecil,[12] Matthew Colless,[5] Warrick J. Couch,[1] Simon P. Driver,[4] Christoph Federrath,[5] Caroline Foster,[1] Michael Goodwin,[1] Elise J. Hampton,[5] A. M. Hopkins,[1] D. Heath Jones,[13] Iraklis S. Konstantopoulos,[1,14] J.S. Lawrence,[1] Sergio G. Leon-Saval,[2] Jochen Liske,[15] Ángel R. López-Sánchez,[1,10] Nuria P. F. Lorente,[1] Jeremy Mould,[16] Danail Obreschkow,[4] Matt S. Owers,[1,10] Samuel N. Richards,[1,2,3] Aaron S.G. Robotham,[17] Adam L. Schaefer,[2,1,3] Sarah M. Sweet,[16] Dan S. Taranu,[3,4] Edoardo Tescari,[3,18] Chiara Tonini,[18] and T. Zafar[1]

[1] Australian Astronomical Observatory, 105 Delhi Rd, North Ryde, NSW 2113, Australia
[2] Sydney Institute for Astronomy, School of Physics, A28, The University of Sydney, NSW, 2006, Australia
[3] ARC Centre of Excellence for All-Sky Astrophysics (CAASTRO)
[4] International Centre for Radio Astronomy Research, University of Western Australia, 35 Stirling Highway, Crawley WA 6009, Australia
[5] Research School of Astronomy and Astrophysics, Australian National University, Canberra, ACT 2611, Australia
[6] Cahill Center for Astronomy and Astrophysics, California Institute of Technology, MS 249-17, Pasadena, CA 91125, USA
[7] Hubble Fellow
[8] Max Planck Institute for Astronomy, Königstuhl 17, 69117 Heidelberg, Germany
[9] School of Mathematics and Physics, University of Queensland, QLD 4072, Australia
[10] Department of Physics and Astronomy, Macquarie University, NSW 2109, Australia
[11] School of Physics, University of New South Wales, NSW 2052, Australia
[12] Dept. Physics and Astronomy, University of North Carolina, Chapel Hill, NC 27599, USA
[13] English Language and Foundation Studies Centre, University of Newcastle, Callaghan NSW 2308, Australia
[14] Atlassian 341 George St Sydney, NSW 2000, Australia
[15] Hamburger Sternwarte, Universität Hamburg, Gojenbergsweg 112, 21029 Hamburg, Germany
[16] Swinburne University, Hawthorn, VIC 3122, Australia
[17] SUPA School of Physics & Astronomy, University of St Andrews, KY16 9SS, Scotland
[18] School of Physics, The University of Melbourne, Parkville, VIC 3010, Australia

ABSTRACT

We present the first major release of data from the SAMI Galaxy Survey. This data release focuses on the emission-line physics of galaxies. Data Release One includes data for 772 galaxies, about 20% of the full survey. Galaxies included have the redshift range $0.004 < z < 0.092$, a large mass range ($7.6 < \log M_*/\mathrm{M}_\odot < 11.6$), and star-formation rates of $\sim 10^{-4}$ to $\sim 10^{1}\ \mathrm{M}_\odot\,\mathrm{yr}^{-1}$. For each galaxy, we include two spectral cubes and a set of spatially resolved 2D maps: single- and multi-component emission-line fits (with dust extinction corrections for strong lines), local dust extinction and star-formation rate. Calibration of the fibre throughputs, fluxes and differential-atmospheric-refraction has been improved over the Early Data Release. The data have average spatial resolution of 2.16 arcsec (FWHM) over the 15 arcsec diameter field of view and spectral (kinematic) resolution $R = 4263$ ($\sigma = 30\,\mathrm{km\,s^{-1}}$) around H$\alpha$. The relative flux calibration is better than 5% and absolute flux calibration better than ±0.22 mag, with the latter estimate limited by galaxy photometry. The data are presented online through the Australian Astronomical Observatory's Data Central.

Keywords: galaxies: general; astronomical data bases: surveys

1. INTRODUCTION

Our textbooks provide a reasonable picture of how the first dark matter structures assembled out of the primordial matter perturbations (Peacock 1999; Mo et al. 2010). But just how gas settled into these structures to form the first stars and galaxies, and how these evolved to provide the rich diversity of galaxies we see around us today, remains an extremely difficult problem to unravel.

Over the past twenty years, imaging surveys from the Hubble Space Telescope (far field) and the Sloan Digital Sky Survey (near field) have been particularly effective in identifying evolution of galaxy parameters with cosmic time and with environment across large-scale structure. This has been matched by extensive surveys using multi-object spectroscopy (e.g. York et al. 2000; Colless et al. 2001; Driver et al. 2011) that have usually provided a single spectrum within a fixed fibre aperture at the centre of each galaxy; spatial information must be drawn from multi-wavelength broadband images.

It has long been recognized that large-scale multi-object spectroscopic surveys do not provide a complete picture of galaxies. The complexity of galaxies cannot be captured with a single average or central spectrum. Three-dimensional imaging spectroscopy, or integral-field spectroscopy (IFS) is needed to quantify each galaxy.

Driven by pioneering work using Fabry-Perot interferometry (Tully 1974) and lenslet arrays (Courtes et al. 1988), IFS has exploited the plunging costs of large-area detectors to dominate extra-galactic studies today (e.g.

andrew.green@aao.gov.au
†How each author contributed to the paper is listed at the end.

Hill 2014). The first generation of IFS surveys, sampling 10s to 100s of galaxies, have only recently completed. Examples include ATLAS^{3D} (Cappellari et al. 2011a), CALIFA (Sánchez et al. 2012) and SINS (Förster Schreiber et al. 2009). These surveys demonstrated that there is much to learn from both the stellar and gaseous components in data of this kind. However, these surveys all used instruments that target individual galaxies one at a time and are, therefore, not optimal for surveying thousands of galaxies. To move beyond catalogues of a few hundred requires effective multiplexing.

Multiplexing IFS has only recently become possible. The FLAMES instrument on the VLT (Pasquini et al. 2002) was the first, with 15 integral-field units (IFUs) each having 20 spatial resolution elements in a 2×3 arcsec field of view.

The two main approaches to IFS are fibre-based and slicer-based systems. Slicers have higher sensitivity below 400 nm and in the infrared as shown by the KMOS instrument on the VLT (Sharples et al. 2013); they also have excellent performance over narrow fields of view, particularly when assisted by adaptive optics (NIFS; McGregor et al. 2003). However, fibres ease deployment of IFUs over wide fields of view and allow the spectrograph to be mounted on the floor rather than on the telescope, simplifying design and improving stability. Fibre based systems are therefore preferred for wide-field, multi-object IFS in the optical bands.

With the aim of carrying out IFS surveys targeting thousands of galaxies, we developed the Sydney/AAO Multi-object Integral-field spectrograph (SAMI; Croom et al. 2012) on the 3.9m Anglo-Australian Telescope. SAMI provides a multiplex of $\times13$ with each integral-field unit (IFU) having a diameter of 15 arcsec and uses compact fused fibre bundles with minimised cladding between the fibre cores (hexabundles: Bland-Hawthorn et al. 2011; Bryant et al. 2011, 2014). The MaNGA Survey (Bundy et al. 2015) operating on the Apache Point 2.3m Telescope, has also begun a similar project, with an IFU multiplex of $\times16$. Meanwhile, the high-redshift KMOS-3D and KROSS Surveys (Wisnioski et al. 2015; Magdis et al. 2016) are making spatially resolved observations of high redshift galaxies.

Large-scale IFS surveys are uniquely positioned to address a number of the outstanding questions regarding galaxy formation and evolution (Croom et al. 2012; Bland-Hawthorn 2015), including:

- What is the physical role of environment in galaxy evolution?
- What is the interplay between gas flows and galaxy evolution?
- How are mass and angular momentum built up in galaxies?

Mass is thought to be the primary discriminant driving the huge variety of galaxies observed, setting their star formation rate (e.g. Peng et al. 2010, 2012), metallicity (e.g. Tremonti et al. 2004), and morphology. However, in addition to mass, the environment of a galaxy also plays a central role in controlling such properties (e.g. Lewis et al. 2002; Blanton & Moustakas 2009, and Dressler 1980; Cappellari et al. 2011b, respectively). Despite the wealth of data at hand, the physical processes that drive environmental differences are still uncertain. The processes are likely to depend on whether a galaxy is the central galaxy or a satellite in its parent halo, the mass of the parent halo, and local galaxy–galaxy interactions (e.g. Davies et al. 2015). With the broad range of observables available to SAMI, we can directly test which physical processes are at play in environmental transformations.

Gas flow (or lack thereof) in and out of a galaxy controls its evolution with time. Inflows have formed disks, fuelled generation upon generation of new stars, and fed supermassive black holes. In current galaxy-formation theory, galactic-scale outflows explain the difference between the theoretical cold-dark-matter mass function and the observed stellar-mass function (e.g. Baldry et al. 2012). A feedback process with strong mass dependence is needed to resolve this problem. Outflows offer the most promising solution (e.g. Silk & Mamon 2012), and are clearly detected by combining gaseous emission-line ionisation diagnostics with kinematics (e.g. Sharp & Bland-Hawthorn 2010; Fogarty et al. 2012; Ho et al. 2014, 2016a). Gas inflows can be traced using the measurement of misalignment between gas and stellar kinematics (e.g. Davis et al. 2011; Davis & Bureau 2016) and by searching for flattened metallicity gradients (Kewley et al. 2010; Rich et al. 2012).

The mass and angular momentum of a galaxy are most directly probed by its kinematic state. A galaxy's accretion and merger history is central to defining its character, and aspects of this history are encoded in the line-of-sight velocity distributions. By studying the detailed kinematics of galaxies across the mass and environment plane, we unlock a new view of galaxy evolution (Cortese et al. 2016; van de Sande et al. 2017). IFS has defined a new set of morphological classifications in terms of dynamical properties (e.g. Emsellem et al. 2011; Cappellari et al. 2011a), such as the separation into fast rotators (rotation dominated) and slow rotators (dispersion dominated). We aim to understand how these kinematic properties are distributed across the mass–environment plane, and to make direct comparison to simulations that are now becoming available to measure more complex dynamical signatures (e.g. Naab et al. 2014).

IFS surveys have arrived at an auspicious time. Cosmological-scale hydrodynamic simulations can now form thousands of galaxies with realistic properties in $\sim 100\,\mathrm{Mpc}^3$ volumes (e.g. Vogelsberger et al. 2014; Schaye et al. 2015). These simulations allow study of how gas enters galaxies (e.g. Codis et al. 2012) and the impact of feedback (e.g. Genel et al. 2015). Those at higher resolution (e.g. Brooks et al. 2009; Hopkins et al. 2014) are probing details of disk formation, gas flows and feedback, though not yet within a full cosmological context. Direct, detailed comparison of spatially resolved data to these simulations is required to advance our understanding.

In this paper, we present Data Release One (DR1) of the SAMI Galaxy Survey, building on our Early Data Release (EDR) in 2014 (see Allen et al. 2015). We provide data cubes for 772 galaxies and value-added products based on detailed emission-line fitting. Future releases will provide more galaxies and products. In Section 2 we review the SAMI Galaxy Survey itself, including the selection, observations, data reduction and analysis. In Section 3 we describe the Core data being released, with discussion of data quality in subsection 3.4. The emission-line-physics value-added products are described in Section 4. The online database is introduced in Section 5. We summarise in Section 6. Where required, we assume a cosmology with $\Omega_m = 0.3$, $\Omega_\Lambda = 0.7$ and $H_0 = 70\,\mathrm{km\,s^{-1}\,Mpc^{-1}}$.

2. BRIEF REVIEW OF THE SAMI GALAXY SURVEY

The SAMI Galaxy Survey is the first integral-field spectroscopic survey of enough galaxies to characterise the spatially-resolved variation in galaxy properties as a function of both mass and environment. Specific details concerning the survey can be found in papers describing the SAMI instrument (Croom et al. 2012; Bryant et al. 2015), the SAMI-GAMA Sample Target Selection (Bryant et al. 2015), the SAMI Cluster Sample Target Selection (Owers et al. 2017), data reduction (Sharp et al. 2015) and the Early Data Release (Allen et al. 2015). Below we review key aspects of the survey.

2.1. *The SAMI instrument*

SAMI is mounted at the prime focus of the Anglo-Australian Telescope and has 1-degree-diameter field of view. SAMI uses 13 fused optical fibre bundles (hexabundles; Bland-Hawthorn et al. 2011; Bryant et al. 2011, 2014) with a high (75 percent) fill factor. Each bundle combines 61 optical fibres of 1.6 arcsec diameter to form an IFU of 15-arcsec diameter. The 13 IFUs and 26 sky fibres are inserted into pre-drilled plates using magnetic connectors. Optical fibres from SAMI feed into AAOmega, a bench-mounted double-beam optical spectrograph (Sharp et al. 2006). AAOmega provides a selection of different spectral resolutions and wavelength ranges. For the SAMI Galaxy Survey, we use the 580V grating at $3700 - 5700$Å and the 1000R grating at $6250 - 7350$Å. With this setup, SAMI delivers a spectral resolution of $R = 1812$ ($\sigma = 70\,\mathrm{km\,s^{-1}}$) for the blue arm, and $R = 4263$ ($\sigma = 30\,\mathrm{km\,s^{-1}}$) for the red arm at their respective central wavelengths (van de Sande et al. 2017). A dichroic splits the light between the two arms of the spectrograph at 5700Å.

2.2. *Target Selection*

In order to cover a large dynamic range in galaxy environment, the SAMI Galaxy Survey is drawn from two regions with carefully matched selection criteria. The majority of targets are from the Galaxy And Mass Assembly (GAMA) Survey (Driver et al. 2011), and we denote this as the SAMI-GAMA Sample. However, the volume of the SAMI-GAMA region does not contain any massive galaxy clusters, so a second set of targets are drawn from specific cluster fields. This we denote as the SAMI Cluster Sample (Owers et al. 2017).

DR1 includes galaxies only from the SAMI-GAMA Sample and the selection for these targets is described by Bryant et al. (2015). Briefly, the sample is drawn from the 4 × 12-degree fields of the initial GAMA-I survey (Driver et al. 2011), but uses the deeper spectroscopy to $r < 19.8$ of the GAMA-II sample (Liske et al. 2015). The high completeness of the GAMA sample (98.5 per cent) leads to high-reliability group catalogues (Robotham et al. 2011) and environmental metrics (Brough et al. 2013). The GAMA regions also provide broad-band imaging from the ultraviolet to far-infrared (Driver et al. 2016).

The selection limits for the SAMI-GAMA Sample, shown in Figure 1, consist of a set of volume-limited samples with stellar-mass limits stepped with redshift. We select using stellar masses determined from only g- and i-band photometry and redshift, using the relationship given in Eq. 3 of Bryant et al. (2015). This determination is based on the relationship between mass-to-light ratio and colour derived by Taylor et al. (2011), and assumes a Chabrier (2003) initial-mass function.

2.3. *Observing strategy*

Bryant et al. (2015) describe the process of allocating target galaxies to fields for observation.

Our standard observing sequence consists of a flat-field frame (from the illuminated AAT dome) and arc frame, followed by seven object frames each of 1800 s exposure. A flat field and arc are taken to end the sequence. The seven object exposures are offset from one another in a hexagonal dither pattern (see Bryant et al. 2015, Fig.16), with the subsequent frames radially offset from the first exposure by 0.7” in each of six directions 60 degrees apart. This offset is applied based on the most central guide star in the field, using an offset in pixels on the guide camera. Variations in atmospheric refraction and dispersion between different exposures causes the effective offsets to differ for different galaxies on the same field plate. However, the high fill factor of SAMI hexabundles minimises the effect on data quality (see especially Section A). The change in offset across the field is measured as part of the alignment process during data reduction as described in Sharp et al. (2015).

Where possible, twilight-sky frames are taken for each field to calibrate fibre-throughput. Primary spectrophotometric standards are observed each night that had photometric conditions to provide relative flux calibration (i.e. the relative colour response of the system).

2.4. *Data reduction*

Raw telescope data is reduced to construct spectral cubes and other core data products in two stages that are automated for batch processing using the “SAMI Manager”, part of the `sami` python package (Allen et al. 2014). The specifics of both stages are detailed in Sharp et al. (2015). Subsequent changes and improvements to the process are described in section 3 of Allen et al. (2015) and in Section 3.2 below.

The first stage of data reduction takes raw 2D detector images to partially calibrated spectra from each fibre of the instrument, including spectral extraction, flat-fielding, wavelength calibration and sky subtraction. Processing for this stage uses the *2dfdr* fibre data reduction package (AAO software Team 2015) provided by the

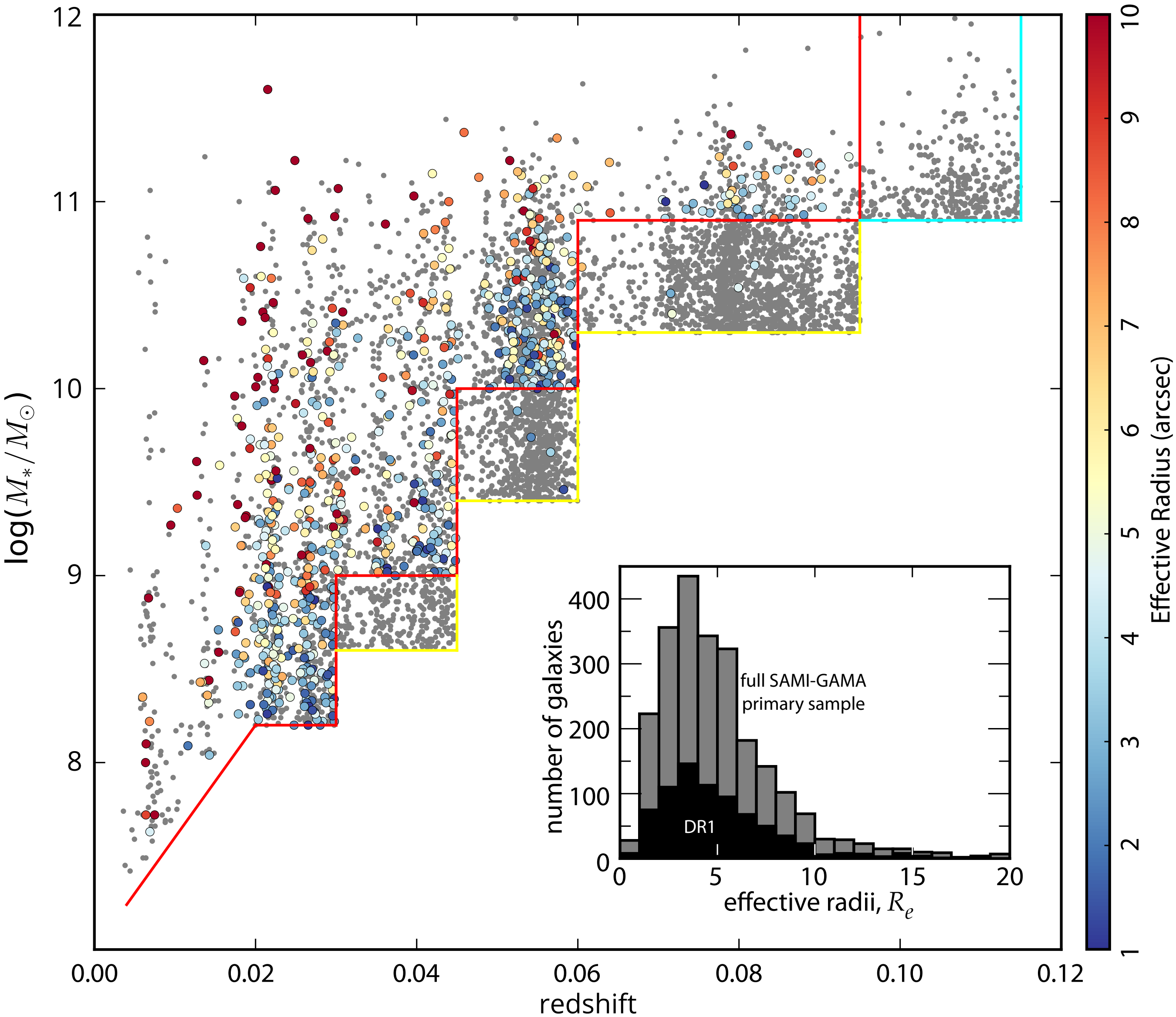

Figure 1. The SAMI-GAMA portion of Galaxy Survey targets in the redshift vs. stellar mass plane. The primary targets lie above the red line, and secondary targets lie above the cyan (higher redshift) or yellow (lower mass) line. Light grey points show the full SAMI-GAMA sample, while the targets comprising DR1 are coloured by effective radius (R_e) in arcsec. The inset histogram illustrates that the R_e distribution of the DR1 galaxies (black) is representative of the full primary sample (grey).

Australian Astronomical Observatory[1]. This stage outputs the individual fibre spectra as an array indexed by fibre number and wavelength, and referred to as "row-stacked spectra" (RSS).

In the second stage, the row-stacked spectra are sampled on a regular spatial grid to construct a 3-dimensional (2 spatial and 1 spectral) cube. Processing for the second stage is done within the `sami` python package (Allen et al. 2014). This stage includes telluric correction, flux calibration, dither registration, differential atmospheric refraction correction and mapping input spectra onto the output spectral cube. The last of these stages uses a drizzle-like algorithm (Fruchter & Hook 2002; Sharp et al. 2015). The spectral cubes simplify most subsequent analysis because the cube can be read easily into various packages and programming languages, and spatial mapping of the data is straightforward. However, in creating the spectral cube, additional covariance between spatial pixels is introduced that must be correctly considered when fitting models and calculating errors (Sharp et al. 2015).

[1] Different versions of *2dfdr* are available, along with the source code for more recent versions at `http://wwww.aao.gov.au/science/software/2dfdr`

2.5. *Comparing SAMI with other large IFS Surveys*

Spatial resolution— The SAMI Galaxy Survey has less spatial resolution elements per galaxy than most first generation IFS surveys. First generation surveys were based on instruments with a single IFU with a large field of view on the sky and many spatial samples. For example, CALIFA uses the PPAK fibre bundle (Kelz et al. 2006) that contains 331 science fibres and uses this bundle to target a single galaxy at a time. In contrast, SAMI has 793 target fibres, a factor of ×2.4 more, but distributes them over 13 targets, with a much smaller field of view per IFU. The ATLAS^{3D} and CALIFA Surveys target lower redshift galaxies better matched in size to their larger IFUs, leading to higher spatial resolution. Therefore, these first generation surveys continue to serve as a benchmark for local (< 100 Mpc) galaxies, while second generation surveys will provide much larger samples of slightly more distant galaxies (typically > 100 Mpc).

Spectral resolution— In the neighbourhood of the Hα emission line, the SAMI Galaxy Survey has higher spectral resolution than most other first- and second-generation surveys. In the blue arm the large number of spectral features visible drives the survey design to broad wavelength coverage (3700–5700Å), leading to a resolution of $R \simeq 1812$. However, in the red arm, by limiting spectral coverage to a ∼ 1100Å region around the Hα emission line we can select a higher spectral resolution, $R \simeq 4263$. This selection is distinct from most other surveys, such as CALIFA and MaNGA, with $R \simeq 850$ and $R \simeq 2000$ respectively around the Hα line. Therefore, analyses based on SAMI data can better separate distinct kinematic components (e.g. in outflows; see Ho et al. 2014, 2016a), can more accurately measure the gas velocity dispersion in galaxy disks (Federrath et al. 2017), and can investigate the kinematics of dwarf galaxies. The trade-off for the higher spectral resolution in the red arm is more limited spectral coverage, that only extends to ∼ 7400Å, whereas MaNGA reaches to ∼ 1 μm.

Environment measures— The SAMI Galaxy Survey also benefits from more complete and accurate environmental density metrics than other IFS surveys. The GAMA Survey has much greater depth ($r < 19.8$ vs $r < 17.8$) and spectroscopic completeness (> 98 per cent vs ≃ 94) than the SDSS on which the MaNGA Survey is based (Driver et al. 2011 and Alam et al. 2015, respectively). Therefore, GAMA provides several improved environmental metrics over SDSS, including group catalogues and local-density estimates (Robotham et al. 2011 and Brough et al. 2013, respectively). For example, 58 per cent of primary Survey targets are members of a group identified from GAMA (containing two or more galaxies based on a friends-of-friends approach–see Robotham et al. 2011), but only 15 per cent are members of a group identified from SDSS (Yang et al. 2007).

Range in mass— The SAMI Survey provides a broader range in mass of galaxies than MaNGA at the expense of more variability in the radial coverage of galaxies. Our target selection aims to be 90 percent complete above the stellar-mass limit for each redshift interval targeted while covering a large range in stellar mass ($8 \lesssim \log(M_*/\mathrm{M}_\odot) \lesssim 11.5$). This selection results in a more extensive sampling of low-mass galaxies than previous surveys. It also differs from the MaNGA selection, which targets galaxies in a relatively narrow luminosity range at each redshift. The MaNGA selection leads to less variability in the radial extent of the data relative to galaxy size.

Sampling of galaxy clusters— The Survey's cluster sample is also unique among IFS surveys. Massive clusters are rare, so volume-limited samples typically include few galaxies belonging to these extreme environments. However, only in clusters are the extremes of environmental effects demonstrated on galaxy evolution. With the Survey's cluster sample, one can trace in detail the evolution of galaxies in the densest environments. Other programs have targeted individual clusters for IFS observations (e.g. Cappellari et al. 2011a; Houghton et al. 2013; D'Eugenio et al. 2013; Scott et al. 2014), but the SAMI cluster sample is the most comprehensive IFS study of clusters yet attempted. The SAMI Galaxy Survey sample includes eight different clusters (APMCC0917, A168, A4038, EDCC442, A3880, A2399, A119 and A85), allowing investigation of variability between clusters. Part of the Survey includes new (single-fibre) multi-object spectroscopy of these clusters to ascertain cluster membership, mass, and dynamical properties (Owers et al. 2017).

Table 1
SAMI-GAMA Sample primary and filler targets (see Figure 1) observed by end of 2016 and their DR1 release.

	No. in catalogue	Galaxies observed	Galaxies in this Release
Primary targets	2404	1267	763
Filler targets	2513	44	9

3. CORE DATA RELEASE

The galaxies included in DR1 are drawn exclusively from the SAMI-GAMA Sample. The included core data products are the regularly gridded flux cubes (spectral cubes). All of the core data included have met minimum quality standards, and the quality of the final data has been measured with care.

3.1. *Galaxies included in DR1*

Galaxies in DR1 are drawn from all 832 galaxies observed in the SAMI-GAMA sample through June, 2015 (AAT semesters 2013A to 2015A). This includes all galaxies in the Survey's EDR (but the data for those galaxies have been reprocessed for this Release). Table 1 shows how the DR1 galaxy numbers compare to the current progress of the SAMI Galaxy Survey in the GAMA regions. The distribution of these targets in the stellar mass–redshift plane, on the sky and in the star formation rate–stellar mass plane can be seen in Figures 1, 2 and 3, respectively.

We have not included some observed galaxies in DR1 for quality control reasons. From the 832 galaxies, we removed those with:

- fewer than 6 individual exposures meeting the minimum standard of transmission greater than 0.65 and seeing less than 3 arcsec FWHM (48 galaxies removed); and
- individual observations that span more than one month for a single field and have differences in their heliocentric velocity frames of greater than 10 km/s (12 galaxies removed).

After removing observations that did not meet these data quality requirements, 772 galaxies remain.

Galaxies included in DR1 may have a small bias towards denser regions over the full field sample. The order in which galaxies are observed over the course of the

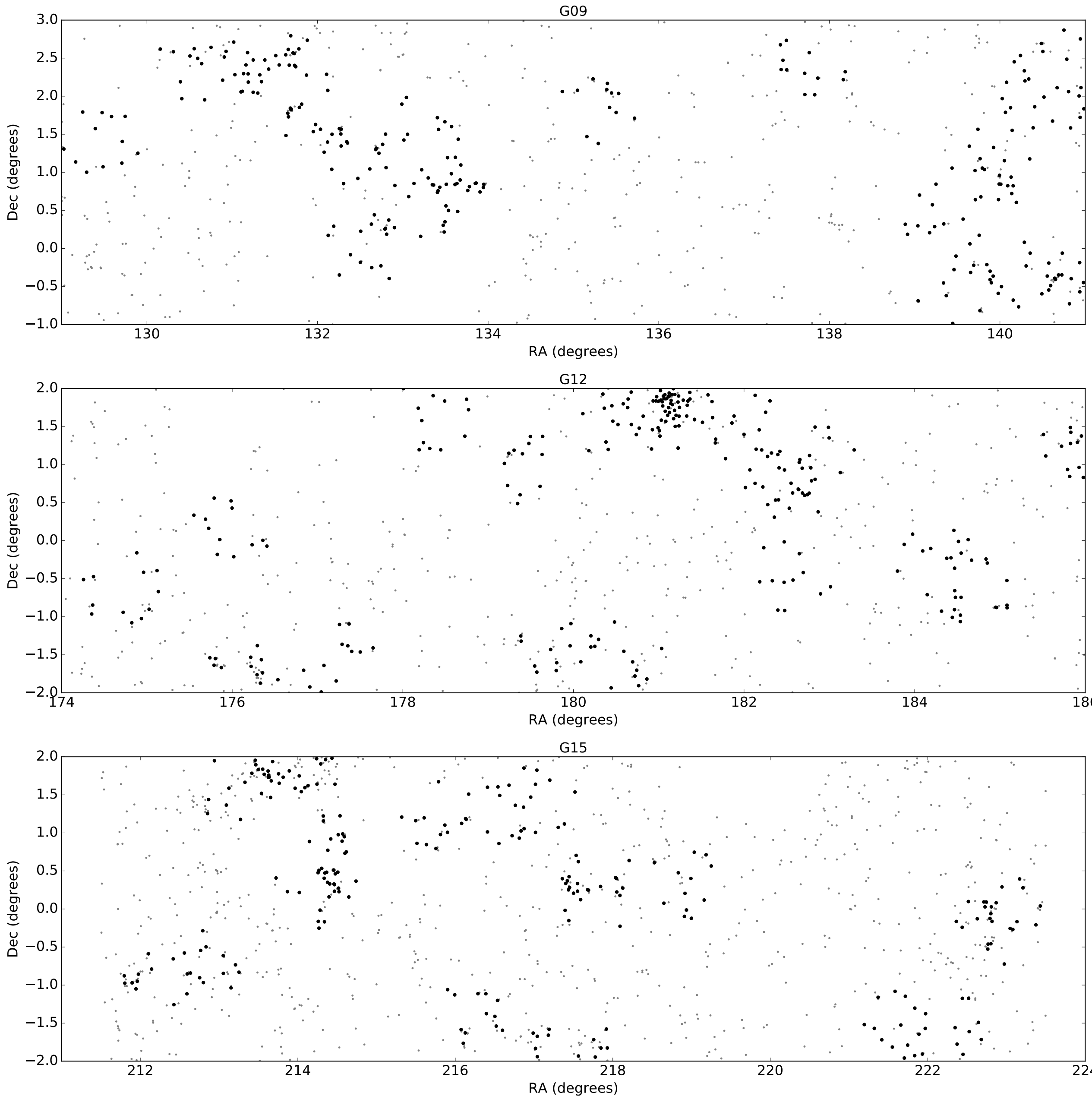

Figure 2. Distribution on the sky of the SAMI-GAMA Sample, covering GAMA regions G09, G12, and G15. The primary targets of the complete field sample are shown by the small grey points, targets included in this DR1 are shown in black.

Survey is set by the tiling process, which allocates galaxies to individual observing fields. Tiling is based only on the sky distribution of galaxies—not their individual properties. Initial tiles are allocated preferentially to regions with higher sky density to maximize the efficiency of the Survey over all. Figure 2 shows the three GAMA-I fields (G09, G12 and G15) and the sky distribution of galaxies in this data release compared with the overall SAMI field sample.

DR1 galaxies are distributed across the full range of the primary sample in redshift, stellar mass and effective radius as illustrated in Figure 1. A Kolmogorov–Smirnov test indicates that the DR1 sample has the same effective radius distribution as the SAMI field sample (D-statistic=0.025, p-value=0.85). However there is a difference in the distribution of stellar mass (D-statistic=0.08, p-value=0.001), such that lower mass galaxies are slightly over represented in the DR1 sample.

3.2. *Changes in data reduction methods since the Early Data Release*

For DR1 we use the `sami` python package snapshot identified as Mercurial changeset `0783567f1730`, and *2dfdr* version 5.62 with custom modifications. The version of *2dfdr* is the same as for our Early Data Release (Allen et al. 2015), and all of the modifications are described by Sharp et al. (2015). These changes have

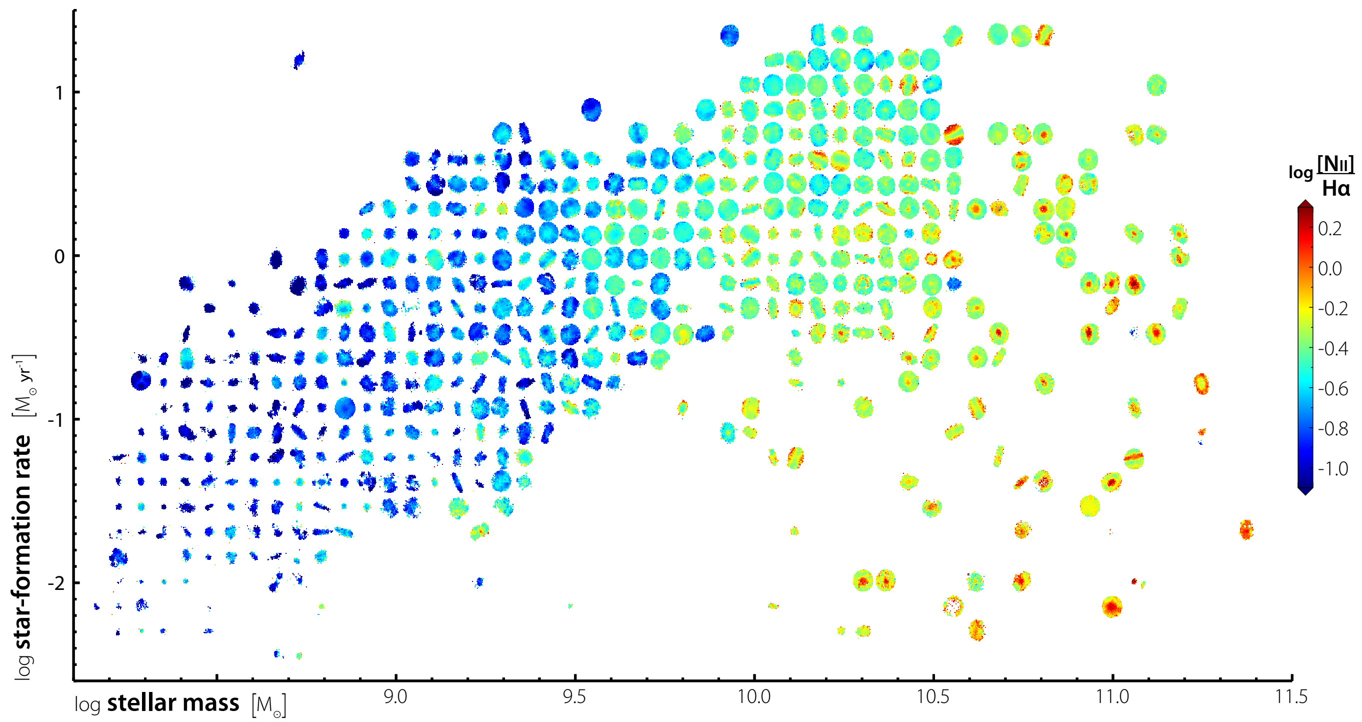

Figure 3. The spatially-resolved maps of [NII]/Hα within 15 arcsec diameter of DR1 galaxies are arrayed by stellar mass and star-formation rate. Not all in DR1 appear because some have insufficient [NII] and/or Hα flux for their S/N ratio to exceed 3 across their extent. Some maps have been shifted slightly to avoid overlap, so stellar masses and star-formation rates shown are indicative, not exact.

been integrated into subsequent public release versions of *2dfdr*. Changes in the `sami` package are described in the rest of this section.

3.2.1. *Fibre throughput calibration*

To achieve good flux calibration and uniform image quality, the relative throughput of each of the 819 fibres (including 26 sky fibres) must be normalised to a common value. We have improved the approach for normalising the fibre throughputs over that used in our EDR.

The fibre-throughput calibration used in our EDR had two shortcomings that limited data quality, particularly from the blue arm of the spectrograph. In our EDR, the relative throughput of individual fibres was primarily determined from the integrated flux in the night-sky lines for long exposures, and from the twilight flat-fields for short exposures. However, the blue data (3700–5700Å) include only one strong night sky line, 5577Å, so are particularly susceptible to two problems. First, sky lines are occasionally impacted by cosmic rays, leading to poor throughput estimates for individual fibres. Second, the limited photon counts in the sky line limits the estimates of the relative throughput to $\simeq 1-2$ per cent.

For DR1 the relative fibre throughputs were calibrated from either twilight flat-field frames, or from dome flat-field frames for fields where no twilight flat was available. The night sky spectrum was then subtracted using this calibration. If the residual flux in sky spectra was excessive (mean fractional residuals exceeded 0.025), then the fibre throughputs were remeasured using the integrated flux in the night-sky lines (as in the EDR). If all sky lines in a fibre were affected by bad pixels (typically only an issue for the blue wavelength range, which covers only a single sky line), then the mean fibre-throughput calibration derived from all other frames of the same field was adopted. The sky subtraction was then repeated with the revised throughput values. The method that provided the final throughput calibration is listed with the cubes in the online database. This approach ensures that, for the calibration options available, the best option is used to calibrate the fibre throughputs.

3.2.2. *Flux calibration*

The flux calibration process has been improved over our EDR to better account for transparency changes between individual observations of a field and improve overall flux calibration accuracy. In our EDR, the absolute flux calibration was applied after forming all cubes for a field of 12 galaxies and 1 secondary standard star. All objects in the field were scaled by the ratio of the field's secondary standard star observed g-band flux to the SDSS photometry *after combining individual observations into cubes* (for full details see section 4.4 of Sharp et al. 2015).

For DR1 this scaling has also been applied to each individual RSS frame for a given field *before forming cubes*, i.e., the scaling is now applied twice. This additional scaling ensures that differences in transparency between individual observations are removed before the cube is formed, which improves the local flux calibration accuracy and removes spatial 'patchiness' in the data. The accuracy of the overall flux calibration is discussed in Section 3.4.3.

3.2.3. *Differential atmospheric refraction correction*

For DR1 we have improved the correction for differential atmospheric refraction over that in our EDR. The atmospheric dispersion is corrected by recomputing the drizzle locations of the cube at regular wavelength intervals (see section 5.3 of Sharp et al. 2015). In our EDR the drizzle locations were recomputed when the accumulated dispersion misalignment reached 1/10th of a spaxel (0.05 arcsec). We found that this frequency caused unphysical 'steps' in the spectra within a spaxel. In DR1 we recalculated the drizzle locations when the accumulated dispersion misalignment reached 1/50th of a spaxel, i.e., five times more often than in the Early Data Release. This significantly reduced the impact of atmospheric dispersion on the local flux calibration within individual spaxels. Section A elaborates on how atmospheric dispersion affects the quality of the data.

3.3. *Core Data Products included*

Several Core data products are included in DR1: flux spectral cubes with supporting information, GAMA catalogue data used for the target selection, and Milky Way extinction spectra.

3.3.1. *Spectral Cubes*

The position–velocity spectral flux cubes are the products most users will value. These cubes are presented with the following supporting data, all sampled on the same regular grid:

variance: The uncertainty of the intensities as a variance, including detector-readout noise and Poisson-sampling noise propagated from the raw data frames.

spatial covariance: co-variance between adjacent spatial pixels introduced by drizzle mapping onto the regular grid. The co-variance and the format of this five-dimensional array are described in section 5.7 of Sharp et al. (2015).

weights: The effective fractional exposure time of each pixel, accounting for gaps between individual fibres, dithering, etc. These are described in section 5.3 of Sharp et al. (2015).

A world-coordinate system (WCS) for each cube is included. This WCS maps the regular grid onto sky- (right ascension and declination) and wavelength-coordinates. The origin of the spatial coordinates in the WCS is defined using a 2D Gaussian fit to the emission in the first frame of the observed dither sequence. The wavelength coordinates are defined in the data-reduction process from arc-lamp frames. The accuracy of the spatial coordinates is discussed in Section 3.4.4 and that of the wavelength coordinate in section 5.1.3 of Allen et al. (2015).

Also provided for each spectral cube are estimates of the point-spread function (PSF) of the data in the spatial directions. The PSF is measured simultaneously with data collection using the secondary standard star included in each SAMI field. We provide the parameters of a circular-Moffat-profile fit to that star image (i.e. the flux calibrated red and blue star cubes summed over the wavelength axis). The Moffat profile has form

$$f = \frac{\beta - 1}{\pi\alpha^2}\left(1 + \left(\frac{r}{\alpha}\right)^2\right)^{-\beta}. \qquad (1)$$

where α and β parameterize the fit and $r^2 = x^2 + y^2$ is the free variable denoting spatial position (Moffat 1969). The reported PSF is the luminosity weighted average over the full (i.e. red + blue) SAMI wavelength range. With the parameters of the Moffat-profile fit, we also provide the corresponding FWHM, W, as given by

$$W = 2\alpha\sqrt{2^{(1/\beta)} - 1}, \qquad (2)$$

measured in arcseconds. The distribution of measured PSF is discussed in section 5.3.2 of Allen et al. (2015), and is unchanged in DR1.

Finally, for convenience, we include the exact versions of the GAMA data used in the sample selection of the SAMI field sample. Note that in some cases, newer versions of these data are available from the GAMA Survey and should be used for scientific analysis.

3.3.2. *Milky Way dust-extinction correction*

SAMI spectral cubes are not corrected for dust extinction, either internal to the observed galaxy or externally from Milky Way dust. However, we do provide a dust-extinction-correction curve for each galaxy to correct for the latter. Using the right ascension and declination of a galaxy, we determined the interstellar reddening, E(B-V), from the Planck v1.2 reddening maps (Planck Collaboration et al. 2014) and the Cardelli et al. (1989) extinction law to provide a single dust-correction curve for each spectral cube. Note that this curve *has not been applied to the spectral cubes.* To correct a SAMI cube for the effects of Milky Way dust, the spectrum of each spaxel must be multiplied by the dust-correction curve.

3.4. *Data Quality*

We now discuss data quality measurements for the Core data released. Allen et al. (2015) discusses the quality of the data in our EDR, including fibre cross-talk, wavelength calibration, flat-fielding accuracy, and other metrics. Where data quality does not differ between our EDR and DR1, we have not repeated the discussion of Allen et al. (2015). Instead, we discuss the data-quality metrics potentially affected by changes in the data reduction.

3.4.1. *Sky Subtraction Accuracy*

The changes to fibre throughput calibration (see Section 2.4) removes occasional (less than one fibre per frame) catastrophically bad throughputs. It does not change the overall average sky subtraction accuracy, as presented by Allen et al. (2015). The lack of change in sky subtraction precision suggests that fibre throughput and photon counting noise in the blue 5577Å line is not currently a limiting factor in the precision of sky subtraction.

Residuals after subtracting sky-continuum may instead arise from scattered light in the spectrograph. The residuals are shown as a function of wavelength and sky fibre number in Figure 4. To clarify the impact of sky subtraction errors, we sum the residual flux in wavelength bins (20 uniform bins per spectrograph arm). The sum reveals sky residuals that would otherwise be dominated by CCD read noise and photon counting errors in a single 0.5 to 1Å-wide wavelength channel. Figure 4 shows that

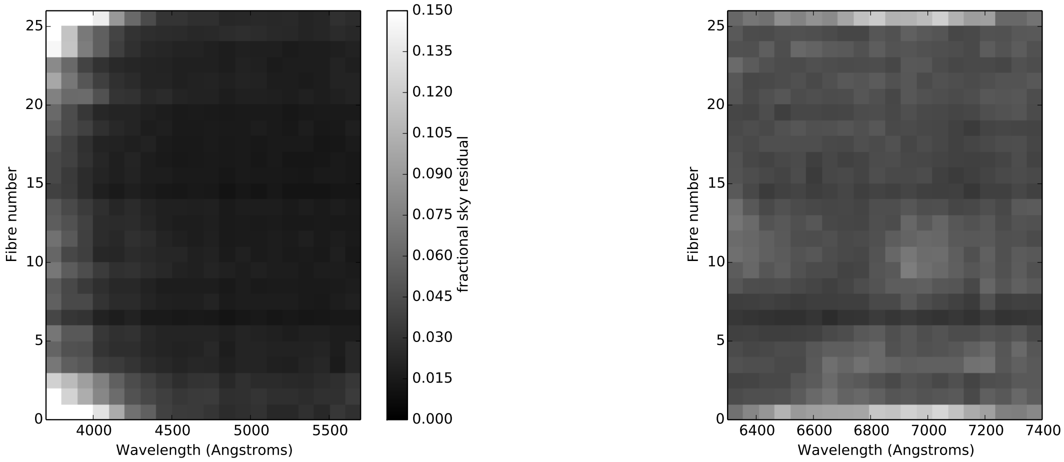

Figure 4. The median fractional sky subtraction residuals as a function of wavelength and fibre number for SAMI sky fibres in the blue (left) and red (right) arms of the spectrograph. The sky fibres are regularly spaced along the SAMI slit, so that sky fibre number also corresponds to approximate location on the AAOmega CCDs. If the sky subtraction was perfect, these residuals would be zero—instead they indicate the likely sky-subtraction residuals in science fibres adjacent to these sky fibres. For each sky fibre shown, the spectral direction is sub-divided into 20 uniform bins, and the residual flux is summed in each of these bins, before determining the median residual (across different observed frames). This reduces the impact of shot noise on the residual estimate and allows us to see systematic variations in sky subtraction. A strong increase in the residual in the left hand corners of the blue CCD are particularly apparent. Note the difference in grey-scale between the two images.

across most of both the blue and red arm CCDs, residuals of the sky-continuum subtraction are ~ 1 percent. However, a strong residual appears at the short wavelength corners of the blue CCD. This is due to a ghost in the spectrograph caused by a double bounce between the CCD and air-glass surfaces of the AAOmega camera corrector lens (Ross Zhelem, private communication). The ghost results in poor fitting of the fibre profiles, which in turn results in poor extraction and then sky subtraction. A solution to this using twilight sky flats to generate fibre profiles has now been developed, but has not been applied to the data in DR1.

3.4.2. *Point spread function*

The spatial PSF is measured by fitting a Moffat function to the reconstructed image of the secondary-standard star in each SAMI field. SAMI fibres have diameter 1.6 arcsec, therefore in seeing $\lesssim 3$ arcsec, the PSF in the individual dithered exposures is under-sampled. Stacking images introduces additional uncertainty from mis-alignment of the seven frames (figure 15 of Allen et al. 2015), and from combining exposures with slightly different seeing. Therefore, the PSF of the final spectral cube is degraded from the PSF of the individual frames. In Figure 5 we compare the FWHM of the reconstructed stellar image (output FWHM) to the mean FWHM of the individual exposures (input FWHM). For small input FWHM (≈ 1 arcsec), output FWHM increases by 50%. This regime is likely dominated by PSF under-sampling. When input FWHM exceeds ≈ 1.5 arcsec, output FWHM is typically 10% larger. No stars have FWHM > 3.0 arcsec as such data is excluded by a quality control limit. In summary, DR1 spectral cubes have a mean PSF of 2.16 arcsec (FWHM).

3.4.3. *Flux Calibration*

The relative flux calibration as a function of wavelength in DR1 is consistent with that in the EDR. By

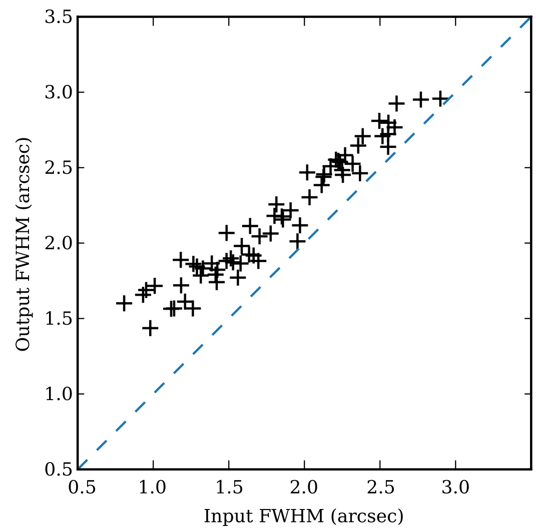

Figure 5. Comparison of the FWHM of the reconstructed secondary standard images (Output FWHM) versus the mean FWHM of the individual dithered exposures (Input FWHM). FWHMs are from Moffat-profile fits. The dashed blue line is the 1:1 relation. The output FWHM is typically larger than the input by 10%. Also shown is the histogram of the Output FWHM. The mean FWHM for DR1 is 2.16 arcsec, and the standard deviation is 0.41 arcsec.

comparing SAMI data with SDSS $g-$ and $r-$band images, Allen et al. (2015) showed that SAMI derived $g-r$ colours have 4.3 percent scatter, with a systematic offset of 4.1 percent, relative to established photometry.

To test the absolute flux calibration, Figure 6 shows the distribution of g-band magnitude differences between the SAMI galaxies and the corresponding Petrosian magnitudes from SDSS. To avoid aperture losses and extrapolations, the distribution is only shown for the 127 SAMI galaxies having Petrosian half-light radius (`petroR50_r`) < 2 arcsec from SDSS. The median offset is -0.07 mag, and the standard deviation is 0.22 mag. This is an im-

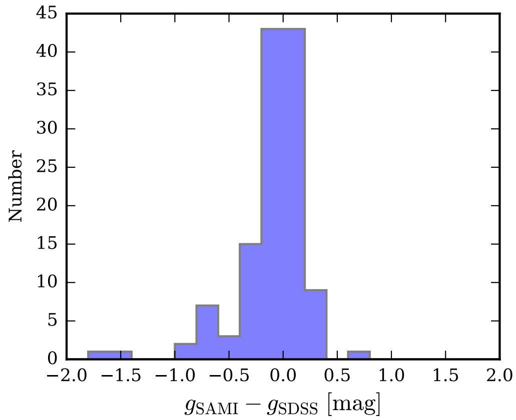

Figure 6. Distribution of the offset in g-band magnitude between the SAMI spectral cube and SDSS magnitudes. Only galaxies with `petroR50_r` < 2 arcsec are included. The mean offset is -0.07 mag and the standard deviation is 0.22 mag.

provement over the standard deviation of 0.27 mag in the EDR. As pointed out by Allen et al. (2015), there is a 0.14 mag scatter between SDSS Petrosian and model magnitudes for our sample, so a considerable fraction of the 0.22 mag scatter is likely due to the inherent limitations in galaxy photometry.

3.4.4. *WCS and Centring of Fibre Bundles in Cubes*

The accuracy of the WCS is limited by the stability and accuracy of the single Gaussian fit on the observation chosen as the reference (typically the first frame, see Section 3.3.1 and section 5.2 of Sharp et al. 2015). By fitting to the individual observed galaxies we lose some robustness. However, we minimize the impact of mechanical errors (plate manufacturing, movement of the connectors within the drilled holes, and uncertainty of the bundle positions) on the WCS accuracy. Examining the data, we have identified three possible failure modes of our approach:

- The fit may identify a bright star within the field of view of the hexabundle instead of the galaxy of interest. Examples include galaxies 8570 and 91961.
- The catalogue coordinate may not correspond to a peak in the surface brightness of the object, such as one with a very disturbed morphology, or for objects where the catalogue coordinate has been intentionally set to be between two galaxies (galaxies with BAD_CLASS=5 in the target catalogue), see Bryant et al. (2015) for details. Examples include galaxy 91999.
- Finally, the circular Gaussian distribution may not represent the true flux distribution well, leading to some instability or bias in the fit result. Examples include large, extended galaxies such as 514260.

In these cases the WCS origin may not be very accurate, and the hexabundle field of view may not be well centred in the output spectral cube.

We carry out two tests to characterise uncertainties in the WCS. The first is an internal check that considers offsets at different stages of the alignment process

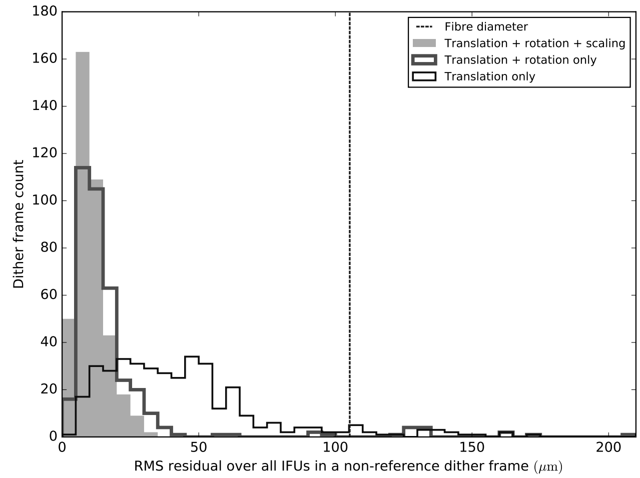

Figure 7. Histograms of the residuals after aligning dither frames. The alignment attempts to simultaneously place bundle centroids of all IFUs in a dither onto the centroids of the 'reference' dither frame. Distributions of residuals are shown for transformations with only a translation, a translation and a rotation, and the full transformation of a translation, a rotation, and a scaling.

to constrain the expected WCS uncertainties. The second cross-correlates the reconstructed SAMI images with SDSS broad-band images to measure the offset between SAMI and SDSS coordinates. These two tests, which we detail in the following paragraphs, suggest that the WCS accuracy is $\lesssim 0.3$ arcsec for most galaxies, except for the failures noted above.

The internal tests to examine WCS uncertainties use alignment offsets to infer bounds on the typical size of the WCS uncertainties. The first dither pointing of an observation aims to centre each galaxy in its bundle. The dither-alignment transformation aligns the galaxy centroid positions in a dither with the galaxy centroid positions in the first ('reference') frame of an observation. Figure 7 shows the RMS of the residuals for all bundles in a dither after the dither was aligned with the reference frame. The residuals are shown for transformations that are translation-only, translation and rotation, and using the full transformation of a translation, rotation and scaling. At least translation is necessary because the dithers are deliberately spatially offset. However rotation is also important in aligning the dither frames to the centre of the cubes as the SAMI instrument plate holder has a small (~ 0.01 degrees) bulk rotation away from its nominal orientation. This rotation suffices to generate offsets from the nominal bundle centres of up to ~ 1 arcsec at the edge of the field of view. A further improvement is gained using the modification of the plate scale, due to differential atmospheric refraction causing small positional shifts over the course of an observation. The mean RMS of $\sim$11 μm (0.16 arcsec) for the full transformation reflects how accurately the data are spatially combined for a typical galaxy and hence provides a lower limit to the WCS uncertainty.

The cross-correlation test of the WCS accuracy compares the spatial flux distribution of the final, reconstructed SAMI cubes to SDSS g-band images. Each cube is multiplied by the SDSS-g-band-filter response and then summed spectrally. The resulting image is then cross-correlated with an SDSS g-band image. These

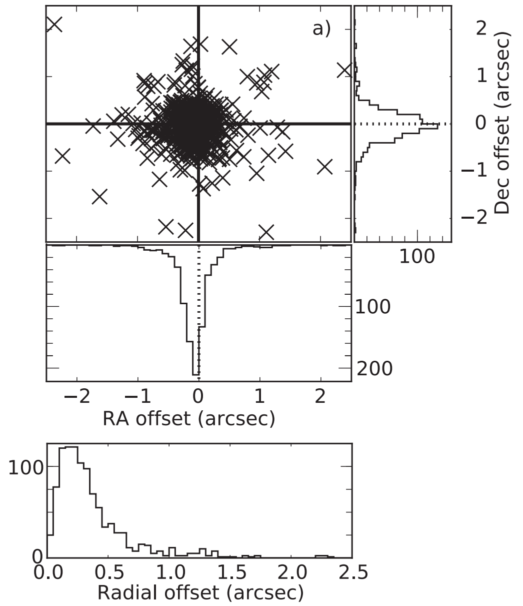

Figure 8. The difference between SAMI and SDSS astrometric solutions based on cross-correlation of images. (top) The distribution of RA and declination differences between SAMI and SDSS, with histograms of the differences in declination and right ascension along the axes. (bottom) Histogram of the distribution of differences in radial offset.

SDSS images are centred on the expected coordinates of the galaxy (based on the GAMA input catalogue), are 36×36 arcsec in size, and have been re-sampled to the same 0.5 arcsec pixel scale as the SAMI cubes. The cross-correlation offset (measured using a fit to the peak in the cross-correlation image) is then the difference between the SAMI WCS and the SDSS WCS. These differences are shown in Figure 8. Outliers in most cases are caused by the cross-correlation centring on bright stars that are present in the SDSS image, but not in the SAMI field of view. Visual checks of outliers also identified five galaxies with gross errors in their SAMI cube WCS, caused by the data reduction centroiding on a bright star in the SAMI field of view rather than the target galaxy (catalogue IDs 8570, 91961, 218717, 228104 and 609396). When outliers are removed using an iterative 5σ clipping (that removes 7.7 per cent of coordinates), the mean of the remaining differences is -0.074 ± 0.020 arcsec in right ascension and -0.048 ± 0.037 arcsec in declination. The root-mean-square scatter is 0.18 arcsec in right ascension and 0.27 arcsec in declination. This test suggests a typical radial WCS error of 0.32 arcsec.

Given that the result of the measurement of the WCS uncertainty in the cross-correlation test is consistent with the bounds suggested by the internal tests, we expect that it is representative of the actual uncertainty in our WCS for most targets. The targets subject to one of the failures mentioned above will have a much larger error in their WCS (no attempt has been made to correct these failures).

3.5. *Impact of aliasing from sampling and DAR on SAMI data*

The combined effects of DAR and limited, incomplete spatial sampling can cause the PSF of IFS data to vary both spatially and spectrally within a spectral cube, an effect we call "aliasing". We describe this in the Appendix, but Law et al. (2015) also provide an excellent discussion. Aliasing can cause issues in comparing widely separated parts of the spectrum on spatial scales comparable to, or smaller than, the size of the PSF. Examples are spectral colour and ratios of widely spaced emission lines. We therefore check the impact of aliasing on our data and discuss options for reducing this impact.

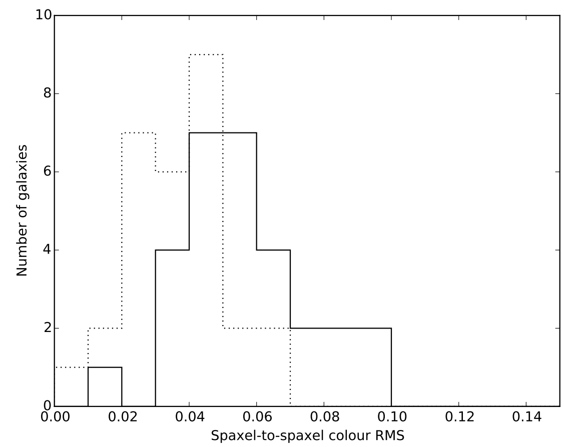

Figure 9. Histogram of RMS scatter in colour between spaxels that are 0.5×0.5 (solid line) or 1.0×1.0 (dotted line) arcsec in size. Galaxies tested are chosen to be passive with uniform colour and the RMS is calculated independently for each galaxy.

To test the impact of aliasing in SAMI data, we check the variation in colour within galaxies expected to have uniform colour across their extent. Uniform colour galaxies are chosen to be passive (no significant emission lines) and to have weak (or flat) stellar population gradients. Using only spaxels in the blue SAMI cubes that have a median $S/N > 15$, we smooth them with a Gaussian kernel in the spectral direction ($\sigma = 15$Å) to reduce noise, and then sum the flux in two bands at wavelengths 3800–4000Å and 5400–5600Å. These bands are chosen to be narrower than typical broad-band filters, but be more sensitive to the size of the aliasing effects (see Appendix). For each galaxy we then estimate the RMS scatter in the colour formed by the ratio of the flux in these two bands. Figure 9 shows the distribution of RMS scatter measurements in the spaxel-to-spaxel spectral colour for 29 galaxies. For the default 0.5×0.5-arcsec spaxels (solid line in Figure 9) the median scatter is 0.052 and the 5th–95th percentile range is $0.033 - 0.093$. Summing spaxels 2×2 within the cubes so that we have 1.0×1.0-arcsec spaxels (dotted line in Figure 9) leads to a reduced RMS with median value of 0.035 and the 5th–95th percentile range is $0.012 - 0.061$. The reduction in scatter when the data are binned to larger spaxels is consistent with the scatter being caused by aliasing in DAR re-sampling.

Aliasing from DAR re-sampling can also affect line-ratios. The ratio of the Hα and Hβ emission lines is typically used to estimate dust attenuation. Variations in the PSF at these two wavelengths causes the ratio to reflect not only the true ratio of the two lines, but also the difference in the PSF between the two wavelengths. The later effect will be most pronounced where there is a sharp change in flux with spatial position in either of the two lines (such as near an unresolved H II region). In such a region, there will be variations pixel-to-pixel (smaller than the PSF) that are larger than would be indicated by the variance information of the data alone.

One possible method for reducing the impact of aliasing on SAMI data is to smooth it. For example, smoothing the Hα-Hβ line ratio map by a 2D Gaussian kernel of Gaussian-σ of 0.5 arcsec (one spatial pixel) and truncated to 5×5 pixels removes most of the variation caused by aliasing without greatly affecting the output spatial resolution. This smoothing brings the noise properties of the Hα-Hβ line ratio into agreement with Gaussian statistics and significantly reduces variation in the normalised spectra for (point-source) stars. The best choice for the smoothing kernel σ probably ranges between 0.2 and 1 arcsec, depending on the science goal and the level of DAR aliasing associated with the galaxy properties and observational conditions. Smoothing should only be necessary when no other averaging is implicit in the analysis (e.g. smoothing is not necessary for measuring radial gradients).

Alternative data reconstruction schemes may reduce the effects of aliasing from the DAR re-sampling. Smoothing options are discussed further in A. Medling et al. (submitted) as they pertain to the emission-line Value Added Products (described briefly in Section 4). In general only results that depend on the highest possible spatial resolution are likely to be sensitive to aliasing.

4. EMISSION-LINE PHYSICS VALUE-ADDED DATA PRODUCTS

With the Core Data Products described above, our DR1 also includes Value-Added Products based on the ionized-gas emission lines in our galaxies. We provide fits for eight emission lines from five ionisation species, maps of Balmer extinction, star-formation masks, and maps of star-formation rate for each galaxy. Examples of these products are shown in Figure 10 for a selection of galaxies spanning the range of stellar masses in DR1.

4.1. *Single- and multi-component emission-line fits*

We have fit the strong emission lines ([O II] 3726,3729, Hβ, [O III] 4959,5007, [O I] 6300, [N II] 6548,6583, Hα, and [S II] 6716,6731) in the spectral cubes with between one and three Gaussian profiles. We fit with the `LZIFU` software package detailed in Ho et al. (2016b). These fits include corrections for underlying stellar-continuum absorption. `LZIFU` produces both a single component fit and a multi-component fit for each spatial pixel of the spectral cube. The latter fits select the optimum number of kinematic components in each spatial pixel.

All lines are fit simultaneously across both arms of the spectrograph. The blue and red spectral cubes have FWHM spectral resolutions of $2.650^{+0.122}_{-0.088}$ Å and $1.607^{+0.075}_{-0.052}$ Å, respectively. Assuming that the kinematic profiles are consistent for all lines, the higher resolution in the red helps to constrain the fits in the blue, where individual kinematic components may not be resolved.

`LZIFU` first fits underlying stellar continuum absorption using the penalized pixel-fitting routine (PPXF; Cappellari & Emsellem 2004), then uses `MPFIT` (the Levenberg-Marquardt least-square method for IDL; Markwardt 2009) to find the best-fit Gaussian model solution.

Our continuum fits combine template spectra of simple stellar populations from the Medium resolution INT Library of Empirical Spectra (MILES, Vazdekis et al. 2010). These spectra are based on the Padova isochrones (Girardi et al. 2000). The selected templates have four metallicities ($[M/\mathrm{H}] = -0.71,\ -0.40,\ 0.0,\ +0.22$) and 13 ages (logarithmically spaced between 63.1 Myr and 15.8 Gyr). In fitting the template spectra to our observed data, Legendre polynomials (orders 2-10) are added (not multiplied) to account for scattered light and other possible non-stellar emission within the observed spectral cubes, and a reddening curve parametrised by Calzetti et al. (2000) is applied. Note that the MILES templates have slightly lower spectral resolution than the red arm of our spectra; therefore, in low-stellar-velocity-dispersion galaxies ($\sigma < 30\,\mathrm{km\,s^{-1}}$), the template may under-estimate the Hα absorption. To account for this and other systematic errors from mis-matched templates, we calculate the expected uncertainty in the Balmer absorption from the uncertainty in stellar-population age as measured from the size of the $\mathrm{D_n}4000$ break. This uncertainty is added into the Balmer-emission-flux uncertainty in quadrature.

Each emission line in each spaxel is fit separately with one, two, and three Gaussian components. In each case, a consistent velocity and velocity dispersion are required for a given component across all lines. For each galaxy, DR1 includes two sets of fits: one that uses a single Gaussian for each line in each spatial pixel ("single component"), another that includes one to three components for each spatial pixel ("recommended components"). Examples of these two fits are shown in Figure 11. For the fits with recommended components, the number of fits included for each spatial pixel is chosen by an artificial neural network trained by SAMI Team members (`LZComp`, Hampton et al. 2016). For the recommended components, we also require that each component has $\mathrm{S/N} \geq 5$ in Hα; if this condition is not met, we reduce the number of components until it does.

The single-component fits include eight maps of line fluxes, and a map each of ionized gas velocity and velocity dispersion. The [O II] 3726,3729 doublet is summed because the blue spectral resolution prevents robust independent measurements of it's components. Flux maps of [O III] 4959 and [N II] 6548 are omitted because they are constrained to be exactly one-third of [O III] 5007 and [N II] 6583, respectively.

The recommended-component fits include maps of the total line fluxes (i.e. the sum of individual components) for each emission line. Additionally, for the Hα line, three maps show fluxes of the individual fit components, and there are three maps each of the velocity and velocity dispersions, which correspond to the individual components of the Hα emission line. The maps showing individual components of Hα flux, velocity, and velocity dispersion are ordered by component width, i.e. first corresponds to the narrowest line and third to the widest. Where there are fewer than three components, higher numbered components are set to the floating point flag `NaN`, as are all maps without a valid fit.

Figure 3 illustrates the value of the emission line fits and the richness of our DR1. It shows how the nature of gas emission changes within galaxies as a function of their stellar mass and star-formation rate. At lower stellar

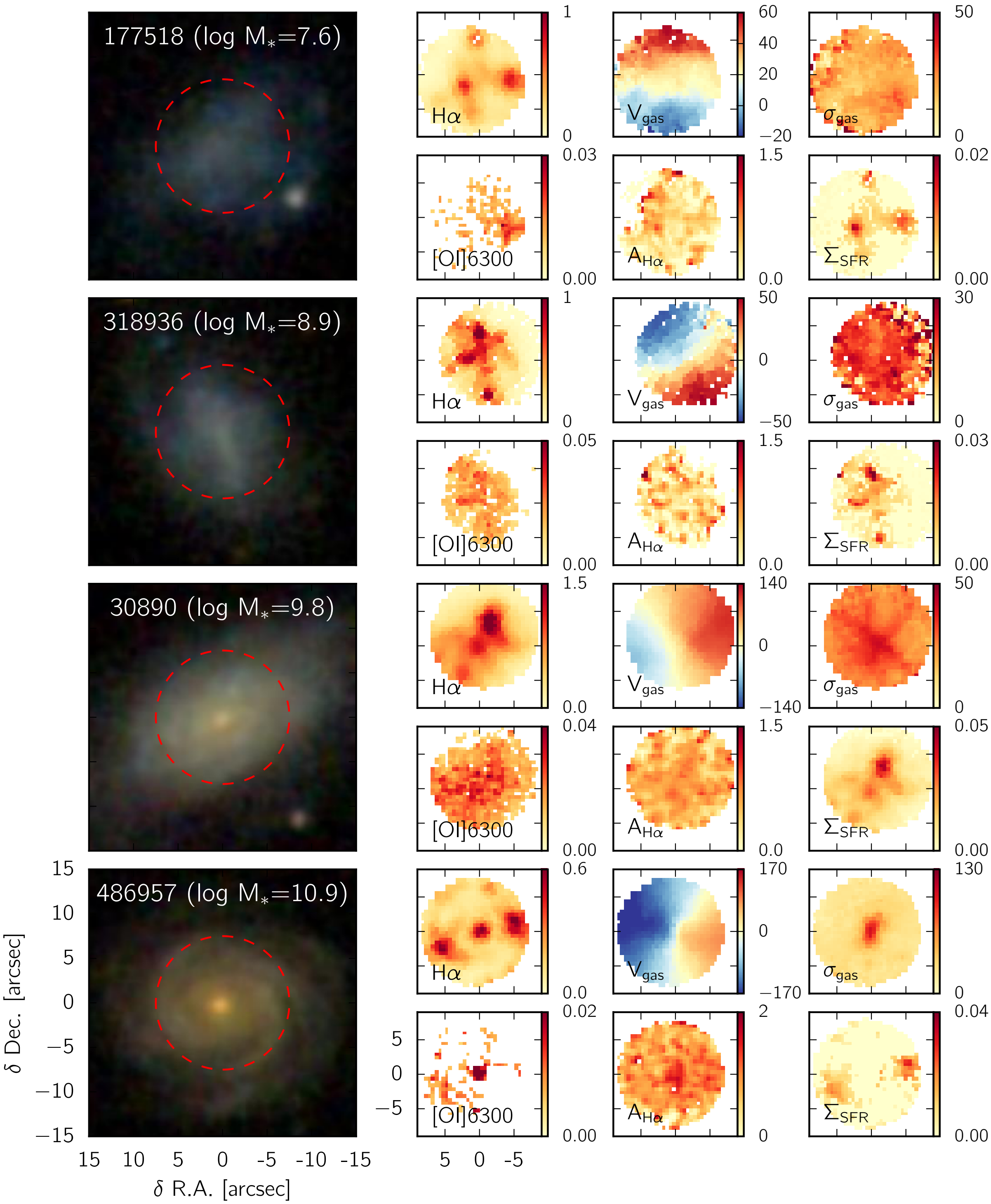

Figure 10. Examples of value-added products for four galaxies spanning the range of stellar masses included in our DR1. The red dashed circles on the SDSS 3-colour images (left) indicate the radius of the SAMI fibre bundle. The small panels show the various value-added products: Hα flux, gas velocity (v_{gas}), gas velocity dispersion (σ_{gas}), [O I]λ6300 flux, Hα attenuation correction factor ($A_{H\alpha}$), and star formation rate surface density Σ_{SFR} maps. The units are 10^{-16} ergs s^{-1} cm^{-2} arcsec^{-2} for the flux maps, km s^{-1} for the kinematic maps, magnitude for $A_{H\alpha}$, and M$_\odot$ yr^{-1} kpc^{-2} for Σ_{SFR}.

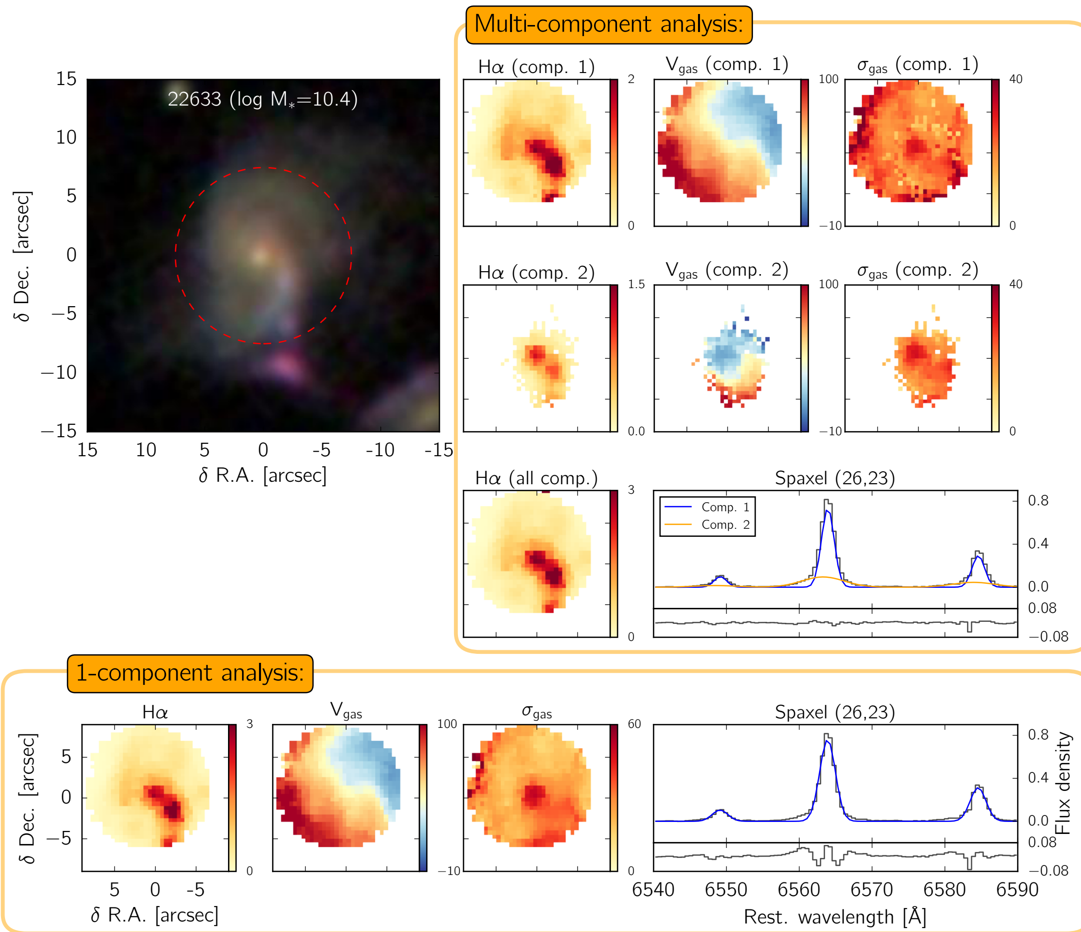

Figure 11. An example comparing multi-component analysis to single-component analysis. The red dashed circle in the SDSS colour image (top left) indicates the SAMI fibre bundle. With the multi-component analysis, we demonstrate that there are two distinct kinematic components in GAMA 22633. The two kinematic components show different velocity dispersions in the spectral fitting panel. The two components also show different Hα distribution (Hα maps for comp. 1 and 2) and velocity structures (v_{gas} maps for comp.1 and 2.). The nature of the second kinematic component cannot be determined with the 1-component analysis that only captures the more dominant narrow kinematic component (bottom row). Including the second kinematic component is necessary to properly model the line profile and reduce the residual.

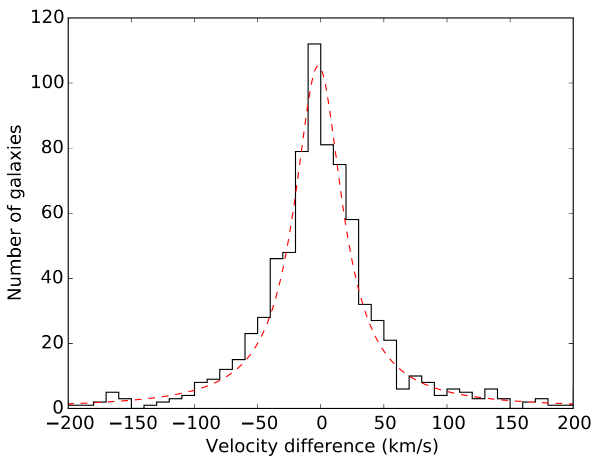

Figure 12. The distribution of rest-frame velocity differences between redshifted catalogued by GAMA and those from LZIFU for SAMI $1R_e$ aperture spectra, both corrected to the heliocentric reference frame. The red dashed line is a Lorentzian fit to the distribution.

masses, emission is driven by star formation, and the gas typically has lower metallicity, which is represented by lower [N II]/Hα ratios (blue). At higher stellar masses, low-star-formation-rate galaxies often host AGN, often resulting in the prominent peak in [N II]/Hα ratio at the centre of the galaxy (red).

Our DR1 includes total-flux model spectral cubes (continuum model plus all fitted emission lines) for direct comparison with the spectral cubes, and maps of quality flags to highlight issues such as bad continuum fits or poor sky subtraction.

4.1.1. *Accuracy of GAMA redshifts and systemic velocities from emission line fits*

LZIFU derived velocities are with reference to the catalogued GAMA redshifts that are listed in the SAMI input catalogue (see Bryant et al. 2015). The GAMA redshifts are on a heliocentric frame and sourced from various surveys such as the main GAMA spectroscopic program (Hopkins et al. 2013), SDSS (York et al. 2000), and 2dFGRS (Colless et al. 2001). To check the velocity scale of the SAMI cubes, we construct aperture spectra by summing across an $1R_e$ ellipse. For SAMI cubes that do not extend to $1R_e$, we sum over the whole SAMI cube. Each aperture spectrum is then fit with LZIFU using exactly the same process as the individual cube spaxels.

Figure 12 shows the velocity difference between the assumed GAMA redshifts and that measured in the aperture spectra. The median difference is $-1.6\,\mathrm{km\,s^{-1}}$ and a robust 1σ range based on the 68–percentile range is $43.9\,\mathrm{km\,s^{-1}}$. The GAMA redshifts used in the SAMI input catalogue were measured using the RUNZ code, and GAMA reports an error on individual RUNZ-derived emission-line redshifts of $33\,\mathrm{km\,s^{-1}}$ from repeat observations (using a robust 68–percentile range; Liske et al. 2015). By subtracting the two in quadrature, we estimate an intrinsic scatter of $35\,\mathrm{km\,s^{-1}}$ for our DR1. This number is an upper limit to the true scatter in SAMI velocity measurements, because it also accounts for differences due to the spatial distribution of Hα. For example, with single-fibre observations targeting a location that is not the dynamical centre of a galaxy, or the SAMI aperture spectrum being dominated by strong Hα flux in the outer parts of galaxies in some cases.

The distribution of velocity differences is well described by a Lorentzian distribution, as found by Liske et al. (2015) for the GAMA velocity uncertainties. The best fit Lorentzian is shown by the red dashed line in Figure 12. The galaxies in the wings of the distribution of velocity differences tend to be those that have lower S/N ratio in the emission line flux.

4.2. *Star Formation Value-Added Products*

Included with DR1 are value added products necessary for understanding the spatially-resolved star formation. These are:

- Maps of Hα extinction: these are derived by assuming a Balmer decrement (Hα/Hβ ratio), unphysical ratios have extinction corrections set to 1 (no correction). Uncertainties in the extinction correction are also provided.
- Masks classifing each spaxel's total emission-line flux as 'star-forming' or 'other': these are derived using the line-ratio classification scheme of Kewley et al. (2006).
- Maps of star-formation rate: these are derived from Hα luminosities and include the extinction and masking above. The conversion factor used is 7.9×10^{-42} $\mathrm{M_\odot\,yr^{-1}(\,erg\ s^{-1})^{-1}}$ from Kennicutt (1998), which assumes a Salpeter initial mass function (Salpeter 1955).

These data products will be described in detail in a companion paper by Anne Medling, et al.

5. ONLINE DATABASE

The data of this Release are presented via an online database interface available from the Australian Astronomical Observatory's Data Central[2]. Data Central is a new service of the Observatory that will ultimately deliver various astronomical datasets of significance to Australian research. Users of the service can find summary tables of the galaxies included in our DR1, browse the data available for individual galaxies, and visualize data interactively online. The service provides for downloading individual and bulk data sets, and a programmatic interface allowing direct access to the data through the HTTP protocol. Also provided are extensive documentation of DR1, the individual datasets within it, and the formatting and structure of the returned data.

Data Central presents data in an object-oriented, hierarchical structure. The primary entities of the database are astronomical objects, such as stars or galaxies. These entities have various measurements and analysis products associated with them as properties. For example, each galaxy in our DR1 is an entity in the database, with properties such as red and blue spectral cubes, LZIFU data products, and star-formation maps. In future, these galaxies may also have data from other surveys associated as properties. This structure is designed to

[2] Data Central's URL is http://datacentral.aao.gov.au

provide an intuitive data model readily discoverable by a general astronomer.

Before deciding to use Data Central to host the Survey's data, the SAMI Team worked on developing our own solution, samiDB (Konstantopoulos et al. 2015). We developed this solution because, at the time, there were no compelling options available to us for organising and making public a data set such as ours. samiDB is designed to require minimum setup and maintenance overhead while providing a long-term stable format. The solution also provides a hierarchical organisation of the data, which has proved valuable as an organisational model. The Team ultimately decided not to use samiDB to present the data because Data Central offers ongoing support for the data archive from the Australian Astronomical Observatory, and hence a better chance that the Survey's data will remain generally and easily available even after the Team has dissolved. However, the hierarchical data model of samiDB has become a central part of the Data Central design.

Further development of Data Central is planned. Most relevant to the SAMI Galaxy Survey will be addition of all data products of the GAMA Survey, enabling seamless querying of SAMI and GAMA as a single data set. Also planned are more tools for interacting with the data online. As this development progresses, the online user interface is expected to continue to evolve, but the data of DR1 (and their provenance), are stable and in their final form on the Data Central service.

6. SUMMARY AND FUTURE

The SAMI Galaxy Survey is collecting optical integral-field spectroscopy for ∼3,600 nearby galaxies to characterise the spatially-resolved variation in galaxy properties as a function of mass and environment. The Survey data are collected with the Sydney/AAO Multi-object Integral-field Spectrograph (SAMI) instrument on the Anglo-Australian Telescope. Survey targets are selected in two distinct samples: a field sample drawn from the GAMA Survey fields, and a cluster sample drawn from eight massive clusters.

With this paper, we release spectral cubes for 772 galaxies from the GAMA sample of the Survey, one-fifth of the ultimate product. We also release Value-Added products for the same galaxies, including maps of emission-line fits, star-formation rate, and dust extinction. These data are well suited to studies of the emission-line physics of galaxies over a range of masses and rates of star formation. The spectral cubes enable a multitude of science in other areas.

The next public data release of the SAMI Galaxy Survey is planned for mid 2018, and will include further data and value-added products.

ACKNOWLEDGEMENTS

The SAMI Galaxy Survey is based on observations made at the Anglo-Australian Telescope. The Sydney/AAO Multi-object Integral-field spectrograph (SAMI) was developed jointly by the University of Sydney and the Australian Astronomical Observatory. The SAMI input catalogue is based on data taken from the Sloan Digital Sky Survey, the GAMA Survey and the VST ATLAS Survey. The SAMI Galaxy Survey is funded by the Australian Research Council Centre of Excellence for All-sky Astrophysics (CAASTRO), through project number CE110001020, and other participating institutions. The SAMI Galaxy Survey website is `http://sami-survey.org/`.

JTA acknowledges the award of a SIEF John Stocker Fellowship. MSO acknowledges the funding support from the Australian Research Council through a Future Fellowship (FT140100255). BG is the recipient of an Australian Research Council Future Fellowship (FT140101202). NS acknowledges support of a University of Sydney Postdoctoral Research Fellowship. SB acknowledges the funding support from the Australian Research Council through a Future Fellowship (FT140101166). JvdS is funded under Bland-Hawthorn's ARC Laureate Fellowship (FL140100278). SMC acknowledges the support of an Australian Research Council Future Fellowship (FT100100457). Support for AMM is provided by NASA through Hubble Fellowship grant #HST-HF2-51377 awarded by the Space Telescope Science Institute, which is operated by the Association of Universities for Research in Astronomy, Inc., for NASA, under contract NAS5-26555. CF gratefully acknowledges funding provided by the Australian Research Council's Discovery Projects (grants DP150104329 and DP170100603). BC is the recipient of an Australian Research Council Future Fellowship (FT120100660).

CONTRIBUTIONS

AWG and SMC oversaw DR1 and edited the paper. SMC is the Survey's Principal Investigator. JBH and SMC wrote the introduction. JB oversaw the target selection, and wrote those parts of the paper. NS wrote sections on the changes to the data reduction, and oversaw the data reduction with JTA and RS. ITH oversaw the emission line fits and produced Figures 10 and 11. AMM ran quality control on the emission line fits, produced the higher-order value-added data products, and coordinated ingestion of these to the database. BG helped coordinate preparation of value-added products for release. MJD and LC oversaw the formatting and preparation of all data for inclusion in the online database. JvdS prepared the survey overview diagram, Figure 3. ADT and SMC measured the accuracy of the WCS information and wrote the corresponding Section 3.4.4. RMM provided heliocentric velocity corrections. FDE and JTA created Figures 5 and 6 and contributed to the data reduction software and to the assessment of the data quality, Section 3.4. AWG, EM, LH, SO, MV, KS, and AMH built the online database serving the data. Remaining authors contributed to overall Team operations including target catalogue and observing preparation, instrument maintenance, observing at the telescope, writing data reduction and analysis software, managing various pieces of team infrastructure such as the website and data storage systems, and innumerable other tasks critical to the preparation and presentation of a large data set such as this DR1.

REFERENCES

AAO software Team. 2015, 2dfdr: Data reduction software, Astrophysics Source Code Library

Alam, S., Albareti, F. D., Allende Prieto, C., Anders, F., Anderson, S. F., Anderton, T., Andrews, B. H., Armengaud, E., et al. 2015, ApJS, 219, 12
Allen, J. T., Croom, S. M., Konstantopoulos, I. S., Bryant, J. J., Sharp, R., Cecil, G. N., Fogarty, L. M. R., Foster, C., et al. 2015, MNRAS, 446, 1567
Allen, J. T., Green, A. W., Fogarty, L. M. R., Sharp, R., Nielsen, J., Konstantopoulos, I., Taylor, E. N., Scott, N., et al. 2014, SAMI: Sydney-AAO Multi-object Integral field spectrograph pipeline, Astrophysics Source Code Library
Baldry, I. K., Driver, S. P., Loveday, J., Taylor, E. N., Kelvin, L. S., Liske, J., Norberg, P., Robotham, A. S. G., et al. 2012, MNRAS, 421, 621
Bland-Hawthorn, J. 2015, in Galaxies in 3D across the Universe, eds. B. L. Ziegler, F. Combes, H. Dannerbauer, & M. Verdugo, vol. 309 of IAU Symposium, 21–28
Bland-Hawthorn, J., Bryant, J. J., Robertson, G., Gillingham, P., O'Byrne, J. W., Cecil, G., Haynes, R., Croom, S., et al. 2011, Optics Express, 19, 2649
Blanton, M. R. & Moustakas, J. 2009, ARAA, 47, 159
Brooks, A. M., Governato, F., Quinn, T., Brook, C. B., & Wadsley, J. 2009, ApJ, 694, 396
Brough, S., Croom, S., Sharp, R., Hopkins, A. M., Taylor, E. N., Baldry, I. K., Gunawardhana, M. L. P., Liske, J., et al. 2013, MNRAS, 435, 2903
Bryant, J. J., Bland-Hawthorn, J., Fogarty, L. M. R., Lawrence, J. S., & Croom, S. M. 2014, MNRAS, 438, 869
Bryant, J. J., O'Byrne, J. W., Bland-Hawthorn, J., & Leon-Saval, S. G. 2011, MNRAS, 415, 2173
Bryant, J. J., Owers, M. S., Robotham, A. S. G., Croom, S. M., Driver, S. P., Drinkwater, M. J., Lorente, N. P. F., Cortese, L., et al. 2015, MNRAS, 447, 2857
Bundy, K., Bershady, M. A., Law, D. R., Yan, R., Drory, N., MacDonald, N., Wake, D. A., Cherinka, B., et al. 2015, ApJ, 798, 7
Calzetti, D., Armus, L., Bohlin, R. C., Kinney, A. L., Koornneef, J., & Storchi-Bergmann, T. 2000, ApJ, 533, 682
Cappellari, M. & Emsellem, E. 2004, PASP, 116, 138
Cappellari, M., Emsellem, E., Krajnović, D., McDermid, R. M., Scott, N., Verdoes Kleijn, G. A., Young, L. M., Alatalo, K., et al. 2011a, MNRAS, 413, 813
Cappellari, M., Emsellem, E., Krajnović, D., McDermid, R. M., Serra, P., Alatalo, K., Blitz, L., Bois, M., et al. 2011b, MNRAS, 416, 1680
Cardelli, J. A., Clayton, G. C., & Mathis, J. S. 1989, ApJ, 345, 245
Chabrier, G. 2003, PASP, 115, 763
Codis, S., Pichon, C., Devriendt, J., Slyz, A., Pogosyan, D., Dubois, Y., & Sousbie, T. 2012, MNRAS, 427, 3320
Colless, M., Dalton, G., Maddox, S., Sutherland, W., Norberg, P., Cole, S., Bland-Hawthorn, J., Bridges, T., et al. 2001, MNRAS, 328, 1039
Cortese, L., Fogarty, L. M. R., Bekki, K., van de Sande, J., Couch, W., Catinella, B., Colless, M., Obreschkow, D., et al. 2016, MNRAS, 463, 170
Courtes, G., Georgelin, Y., Monnet, R. B. G., & Boulesteix, J. 1988, in Instrumentation for Ground-Based Optical Astronomy, ed. L. B. Robinson, 266
Croom, S. M., Lawrence, J. S., Bland-Hawthorn, J., Bryant, J. J., Fogarty, L., Richards, S., Goodwin, M., Farrell, T., et al. 2012, MNRAS, 421, 872
Davies, L. J. M., Robotham, A. S. G., Driver, S. P., Alpaslan, M., Baldry, I. K., Bland-Hawthorn, J., Brough, S., Brown, M. J. I., et al. 2015, MNRAS, 452, 616
Davis, T. A., Alatalo, K., Sarzi, M., Bureau, M., Young, L. M., Blitz, L., Serra, P., Crocker, A. F., et al. 2011, MNRAS, 417, 882
Davis, T. A. & Bureau, M. 2016, MNRAS, 457, 272
D'Eugenio, F., Houghton, R. C. W., Davies, R. L., & Dalla Bontà, E. 2013, MNRAS, 429, 1258
Dressler, A. 1980, ApJ, 236, 351
Driver, S. P., Hill, D. T., Kelvin, L. S., Robotham, A. S. G., Liske, J., Norberg, P., Baldry, I. K., Bamford, S. P., et al. 2011, MNRAS, 413, 971
Driver, S. P., Wright, A. H., Andrews, S. K., Davies, L. J., Kafle, P. R., Lange, R., Moffett, A. J., Mannering, E., et al. 2016, MNRAS, 455, 3911
Emsellem, E., Cappellari, M., Krajnović, D., Alatalo, K., Blitz, L., Bois, M., Bournaud, F., Bureau, M., et al. 2011, MNRAS, 414, 888
Federrath, C., Salim, D., Medling, A., Davies, R., Yuan, T., Bian, F., Groves, B., Ho, I.-T., et al. 2017, MNRAS, in press, arXiv: 1703.09224
Fogarty, L. M. R., Bland-Hawthorn, J., Croom, S. M., Green, A. W., Bryant, J. J., Lawrence, J. S., Richards, S., Allen, J. T., et al. 2012, ApJ, 761, 169
Förster Schreiber, N. M., Genzel, R., Bouché, N., Cresci, G., Davies, R., Buschkamp, P., Shapiro, K., Tacconi, L. J., et al. 2009, ApJ, 706, 1364
Fruchter, A. S. & Hook, R. N. 2002, PASP, 114, 144
Genel, S., Fall, S. M., Hernquist, L., Vogelsberger, M., Snyder, G. F., Rodriguez-Gomez, V., Sijacki, D., & Springel, V. 2015, ApJL, 804, L40
Girardi, L., Bressan, A., Bertelli, G., & Chiosi, C. 2000, A&AS, 141, 371
Hampton, E. J., Groves, B., Medling, A., Davies, R., Dopita, M., Ho, I., Kaasinen, M., Kewley, L., et al. 2016, ArXiv e-prints
Hill, G. J. 2014, Advanced Optical Technologies, 3, 265
Ho, I.-T., Kewley, L. J., Dopita, M. A., Medling, A. M., Allen, J. T., Bland-Hawthorn, J., Bloom, J. V., Bryant, J. J., et al. 2014, MNRAS, 444, 3894
Ho, I.-T., Medling, A. M., Bland-Hawthorn, J., Groves, B., Kewley, L. J., Kobayashi, C., Dopita, M. A., Leslie, S. K., et al. 2016a, MNRAS, 457, 1257
Ho, I.-T., Medling, A. M., Groves, B., Rich, J. A., Rupke, D. S. N., Hampton, E., Kewley, L. J., Bland-Hawthorn, J., et al. 2016b, APSS, 361, 280
Hopkins, A. M., Driver, S. P., Brough, S., Owers, M. S., Bauer, A. E., Gunawardhana, M. L. P., Cluver, M. E., Colless, M., et al. 2013, MNRAS, 430, 2047
Hopkins, P. F., Kereš, D., Oñorbe, J., Faucher-Giguère, C.-A., Quataert, E., Murray, N., & Bullock, J. S. 2014, MNRAS, 445, 581
Houghton, R. C. W., Davies, R. L., D'Eugenio, F., Scott, N., Thatte, N., Clarke, F., Tecza, M., Salter, G. S., et al. 2013, MNRAS, 436, 19
Kelz, A., Verheijen, M. A. W., Roth, M. M., Bauer, S. M., Becker, T., Paschke, J., Popow, E., Sánchez, S. F., et al. 2006, PASP, 118, 129
Kennicutt, Jr., R. C. 1998, ApJ, 498, 541
Kewley, L. J., Groves, B., Kauffmann, G., & Heckman, T. 2006, MNRAS, 372, 961
Kewley, L. J., Rupke, D., Zahid, H. J., Geller, M. J., & Barton, E. J. 2010, ApJL, 721, L48
Konstantopoulos, I. S., Green, A. W., Foster, C., Scott, N., Allen, J. T., Fogarty, L. M. R., Lorente, N. P. F., Sweet, S. M., et al. 2015, Astronomy and Computing, 13, 58
Law, D. R., Yan, R., Bershady, M. A., Bundy, K., Cherinka, B., Drory, N., MacDonald, N., Sánchez-Gallego, J. R., et al. 2015, AJ, 150, 19
Lewis, I., Balogh, M., De Propris, R., Couch, W., Bower, R., Offer, A., Bland-Hawthorn, J., Baldry, I. K., et al. 2002, MNRAS, 334, 673
Liske, J., Baldry, I. K., Driver, S. P., Tuffs, R. J., Alpaslan, M., Andrae, E., Brough, S., Cluver, M. E., et al. 2015, MNRAS, 452, 2087
Magdis, G. E., Bureau, M., Stott, J. P., Tiley, A., Swinbank, A. M., Bower, R., Bunker, A. J., Jarvis, M., et al. 2016, MNRAS, 456, 4533
Markwardt, C. B. 2009, in Astronomical Data Analysis Software and Systems XVIII, ed. D. A. Bohlender, D. Durand, & P. Dowler, vol. 411 of Astronomical Society of the Pacific Conference Series, 251–+
McGregor, P. J., Hart, J., Conroy, P. G., Pfitzner, M. L., Bloxham, G. J., Jones, D. J., Downing, M. D., Dawson, M., et al. 2003, in Society of Photo-Optical Instrumentation Engineers (SPIE) Conference Series, ed. M. Iye & A. F. M. Moorwood, vol. 4841 of Society of Photo-Optical Instrumentation Engineers (SPIE) Conference Series, 1581–1591
Mo, H., van den Bosch, F. C., & White, S. 2010, Galaxy Formation and Evolution
Moffat, A. F. J. 1969, A&A, 3, 455
Naab, T., Oser, L., Emsellem, E., Cappellari, M., Krajnović, D., McDermid, R. M., Alatalo, K., Bayet, E., et al. 2014, MNRAS, 444, 3357
Owers, M. S., Allen, J. T., Baldry, I., Bryant, J. J., Cecil, G. N., Cortese, L., Croom, S. M., Driver, S. P., et al. 2017, MNRAS, accepted for publication
Pasquini, L., Avila, G., Blecha, A., Cacciari, C., Cayatte, V., Colless, M., Damiani, F., de Propris, R., et al. 2002, The Messenger, 110, 1
Peacock, J. A. 1999, Cosmological Physics
Peng, Y.-j., Lilly, S. J., Kovač, K., Bolzonella, M., Pozzetti, L., Renzini, A., Zamorani, G., Ilbert, O., et al. 2010, ApJ, 721, 193
Peng, Y.-j., Lilly, S. J., Renzini, A., & Carollo, M. 2012, ApJ, 757, 4
Planck Collaboration, Abergel, A., Ade, P. A. R., Aghanim, N., Alves, M. I. R., Aniano, G., Armitage-Caplan, C., Arnaud, M., et al. 2014, A&A, 571, A11
Rich, J. A., Torrey, P., Kewley, L. J., Dopita, M. A., & Rupke, D. S. N. 2012, ApJ, 753, 5

Robotham, A. S. G., Norberg, P., Driver, S. P., Baldry, I. K., Bamford, S. P., Hopkins, A. M., Liske, J., Loveday, J., et al. 2011, MNRAS, 416, 2640
Salpeter, E. E. 1955, ApJ, 121, 161
Sánchez, S. F., Kennicutt, R. C., Gil de Paz, A., van de Ven, G., Vílchez, J. M., Wisotzki, L., Walcher, C. J., Mast, D., et al. 2012, A&A, 538, A8
Schaye, J., Crain, R. A., Bower, R. G., Furlong, M., Schaller, M., Theuns, T., Dalla Vecchia, C., Frenk, C. S., et al. 2015, MNRAS, 446, 521
Scott, N., Davies, R. L., Houghton, R. C. W., Cappellari, M., Graham, A. W., & Pimbblet, K. A. 2014, MNRAS, 441, 274
Sharp, R., Allen, J. T., Fogarty, L. M. R., Croom, S. M., Cortese, L., Green, A. W., Nielsen, J., Richards, S. N., et al. 2015, MNRAS, 446, 1551
Sharp, R., Saunders, W., Smith, G., Churilov, V., Correll, D., Dawson, J., Farrel, T., Frost, G., et al. 2006, in Society of Photo-Optical Instrumentation Engineers (SPIE) Conference Series, vol. 6269 of Presented at the Society of Photo-Optical Instrumentation Engineers (SPIE) Conference
Sharp, R. G. & Bland-Hawthorn, J. 2010, ApJ, 711, 818
Sharples, R., Bender, R., Agudo Berbel, A., Bezawada, N., Castillo, R., Cirasuolo, M., Davidson, G., Davies, R., et al. 2013, The Messenger, 151, 21
Silk, J. & Mamon, G. A. 2012, Research in Astronomy and Astrophysics, 12, 917
Taylor, E. N., Hopkins, A. M., Baldry, I. K., Brown, M. J. I., Driver, S. P., Kelvin, L. S., Hill, D. T., Robotham, A. S. G., et al. 2011, MNRAS, 418, 1587
Tremonti, C. A., Heckman, T. M., Kauffmann, G., Brinchmann, J., Charlot, S., White, S. D. M., Seibert, M., Peng, E. W., et al. 2004, ApJ, 613, 898
Tully, R. B. 1974, ApJS, 27, 415
van de Sande, J., Bland-Hawthorn, J., Fogarty, L. M. R., Cortese, L., d'Eugenio, F., Croom, S. M., Scott, N., Allen, J. T., et al. 2017, ApJ, 835, 104
Vazdekis, A., Sánchez-Blázquez, P., Falcón-Barroso, J., Cenarro, A. J., Beasley, M. A., Cardiel, N., Gorgas, J., & Peletier, R. F. 2010, MNRAS, 404, 1639
Vogelsberger, M., Genel, S., Springel, V., Torrey, P., Sijacki, D., Xu, D., Snyder, G., Nelson, D., et al. 2014, MNRAS, 444, 1518
Wisnioski, E., Förster Schreiber, N. M., Wuyts, S., Wuyts, E., Bandara, K., Wilman, D., Genzel, R., Bender, R., et al. 2015, ApJ, 799, 209
Yang, X., Mo, H. J., van den Bosch, F. C., Pasquali, A., Li, C., & Barden, M. 2007, ApJ, 671, 153
York, D. G., Adelman, J., Anderson, Jr., J. E., Anderson, S. F., Annis, J., Bahcall, N. A., Bakken, J. A., Barkhouser, R., et al. 2000, AJ, 120, 1579

APPENDIX

ALIASING CAUSED BY DIFFERENTIAL ATMOSPHERIC REFRACTION CORRECTION AND LIMITED RESOLUTION AND SAMPLING

The effects of differential atmospheric refraction can combine with limited spatial resolution and incomplete sampling to introduce aliasing into the spectra on scales comparable to the PSF. This aliasing is not unique to IFS, though the generally poorer sampling in both resolution and completeness tend to exacerbate the effect. We will use the much simpler case of a long-slit spectrograph to explain the effect.

To understand the impact of aliasing on spectral data in the presence of differential atmospheric refraction, we consider a simple long-slit image[3] of a white continuum source (i.e. one with a flat spectral-energy distribution in wavelength space). The slit has been aligned with the parallactic angle so that atmospheric refraction acts along the length of the slit. For illustrative purposes, we'll consider the fairly extreme example of an object observed at a zenith distance of 60 degrees. Throughout this section, we assume the seeing is Gaussian, with one arcsecond FWHM.

Consider a long-slit image of this object with a spatial scale of one arcsecond per pixel. This image is shown (before correction for DAR) on the left of Figure 13a. Note that the PSF, even before correction, varies considerably along the wavelength axis due to the poor spatial sampling of the data. A correction for DAR is applied by shifting the pixels by the amount of the refraction along the spatial direction and rebinning to the original regular grid. After correction, the image of the object no longer shows a position shift with wavelength (shown on the right in Figure 13a). However, aliasing of the rebinning and sampling are readily visible, causing the individual spectra at each spatial location (shown below the image) to vary within the PSF, and the PSF (shown above the image) to vary with wavelength.

Now, let us extend our example to be a close, 2D analogy to our own 3D spectral cubes. This extended example is shown graphically in Figure 13b. First, we observe the source at several dither positions and air-masses. Second, we introduced gaps in the spatial coverage that are smaller than and within the 1-arcsec pixels (and therefore not readily apparent in the individual frames on the left). The dithering ensures information falling in the gaps in one frame will be picked up in another frame. It also tends to smooth out the aliasing because individual dithers will each have a slightly different aliasing PSF, which will be averaged out in the combination. Finally, to bring our long-slit example closer to the actual process used in SAMI, we add another complication: up-sampling. SAMI fibres are 1.6 arcsec, but we sample the multiple observations onto a 0.5-arcsecond output grid. Note that, in combining these six individual frames, it is also necessary to track the weights of the individual output pixels, which account for the gaps in the input data. This extended example has all the same characteristics and similar sampling dimensions of our actual SAMI data, except that we are working with only one spatial dimension instead of two.

Reviewing the resulting combined, DAR-corrected long-slit image shows that, despite its seeming smoothness, the PSF exhibits subtle but important variations with wavelength and spatial position. This long-slit image is shown on the right of Figure 13b. The image is fairly smooth because up-sampling and several dither positions and airmasses have averaged out some of the aliasing. Yet the subtle differences in the PSF at different wavelengths are still present. These differences are much more apparent in the plot of individual spectra, where the spectrum at each spatial position has been normalised to highlight the relative differences. The spatial location of each of these spectra is shown by the corresponding coloured tick on the right edge of the image. Spectra further from the centre of the PSF (and with lower total flux) tend to have larger relative deviations from the actual spectral shape (this trend matches our analysis of observations of individual stars with SAMI).

[3] For our purposes, a long-slit image is an image of a set of simultaneously observed spectra with spatial coordinate along the slit (chosen to be oriented along the paralactic angle for our examples) on the vertical axis and wavelength coordinates along the horizontal axis.

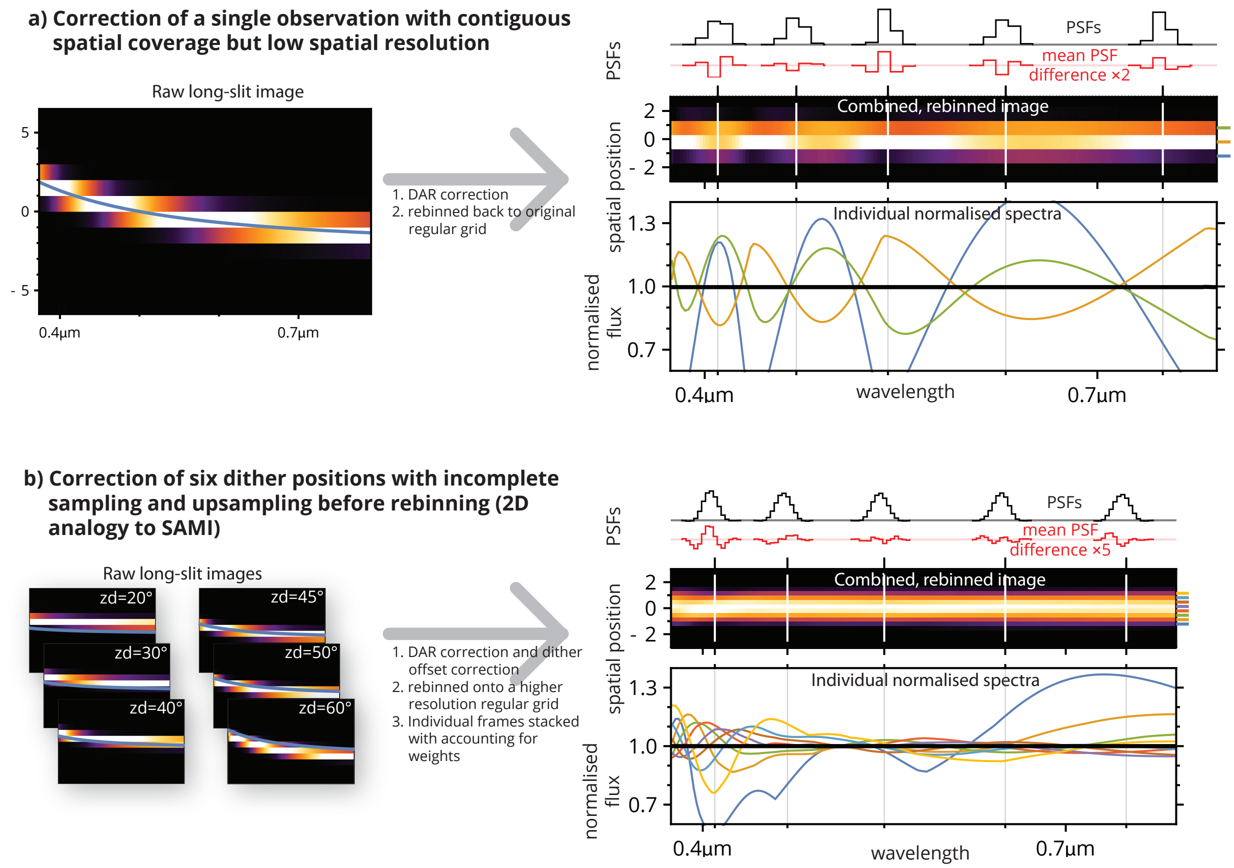

Figure 13. Long slit observations showing the effects of DAR and results of correcting for it in (a) a simple, single long-slit observation at high airmass, and (b) the combination of several long-slit observations at different air masses and dither positions—a close 2D analogy to our 3D data. The example shown in (a) is observed at a zenith distance of 60 degrees. The pixels are 1 arcsec, and the underlying Gaussian PSF has a FWHM of 1 arcsec. In (b), input frames are taken at six air-masses ranging from zenith distance (zd) of 20 to 60 degrees. The underlying PSF is the same, and the spatial pixels are also 1 arcsecond, but the spatial sampling is incomplete. In the rebinning to correct for DAR, the data are up-sampled to 0.33 arcsec pixels before combining.
For each panel: The left-hand side shows the raw long-slit image with a line showing the DAR at the centre of the slit over-plotted. The right-hand side shows the reconstructed long-slit image after DAR correction, including any rebinning. Vertical white lines mark the location of the spatial PSF shown above the image, with the difference from the mean PSF shown in red (scaled up to show detail). The plot below shows individual spectra from the image. The spatial location of each spectrum along the slit is shown by the corresponding coloured tick on the right of the image. These spectra have been normalised to highlight the relative differences in the spectra, which are entirely the result of the aliasing.
NOTE: Some PDF renders will attempt to smooth the pixels shown in this figure; we recommend using Acrobat Reader to see the actual, pixelated images as we intend.

Pixelated (discretely sampled) data observed with DAR present show effects of aliasing. These effects are exacerbated by poor spatial resolution and incomplete sampling. Combining observations with many dithers and different airmasses helps to average the aliasing out. Up-sampling combined with sub-pixel dithering of the observations can also reduce the severity of the aliasing. Aliasing is not typically seen in long-slit data because the PSF is typically well sampled. However, the tension in IFS between spatial sampling and sensitivity, and the incomplete sampling present in many designs has led to noticeable aliasing in IFS data. Although we have only demonstrated the effect in 2D, long-slit data, DAR is only a 2D effect, so our treatment of aliasing readily extends to 3D IFS data.

The general impact of aliasing is that the PSF varies both with spatial and spectral position within either (2D) long-slit images or (3D) spectral cubes. This effect is subtle, and in many cases can be safely ignored without affecting results. There are, however, two important exceptions. The first exception is cases where the PSF must be known to very high accuracy. The second is when comparing data that are widely separated in wavelength, for example emission-line ratios or spatially resolved colours. Any analysis that averages over scales larger than the PSF will not be affected by aliasing, such as measures of radial gradients in galaxies and analysis that requires spatial binning to bring out faint signals.